Measuring ocean total surface current velocity with the KuROS and KaRADOC airborne near-nadir Doppler radars: a multi-scale analysis in preparation for the SKIM mission

Louis Marié, Fabrice Collard, Frédéric Nouguier, Lucia Pineau-Gouillou, Danièle Hauser, François Boy, Stéphane Méric, Peter Sutherland, Charles Peureux, Goulwenn Monnier, et al.

https://doi.org/10.5194/os-2019-77
Preprint. Discussion started: 27 August 2019

Ocean Science
Discussions
Open Access
EGU

Measuring ocean surface velocities with the KuROS and KaRADOC airborne near-nadir Doppler radars: a multi-scale analysis in preparation of the SKIM mission

Louis Marié[1], Fabrice Collard[2], Frédéric Nouguier[1], Lucia Pineau-Guillou[1], Danièle Hauser[3], François Boy[4], Stéphane Méric[5], Charles Peureux[1], Goulven Monnier[6], Bertrand Chapron[1], Adrien Martin[7], Pierre Dubois[8], Craig Donlon[9], Tania Casal[9], and Fabrice Ardhuin[1]

[1]Laboratoire d'Océanographie Physique et Spatiale (LOPS), UMR 6523, Univ. Brest, CNRS, Ifremer, IRD, Brest, France
[2]OceanDataLab, Locmaria Plouzané, France
[3]CNRS, Univ. Versailles St Quentin, Sorbonne Université, LATMOS, France
[4]CNES, Toulouse, France
[5]Institut d'Électronique et de Télécommunication de Rennes (IETR), UMR CNRS 6164, Rennes, France
[6]SCALIAN, Rennes, France
[7]NOC, Southampton, UK
[8]CLS, Ramonville St Agne, France
[9]ESA, Nordwijk, The Netherlands

Correspondence to: Fabrice Ardhuin (fabrice.ardhuin@univ-brest.fr)

Abstract. Surface currents are poorly known over most of the oceans. Satellite-borne Doppler Waves and Current Scatterometers (DWCS) can be used to fill this observation gap. The Sea surface KInematics Multiscale (SKIM) proposal, is the first satellite concept built on a DWCS design at near-nadir angles, and now one of the two candidates to become the 9th mission of the European Space Agency Earth Explorer program. As part of the detailed design and feasibility studies (phase A) funded by ESA, airborne measurements were carried out with both a Ku-Band and a Ka-Band Doppler radars looking at the sea surface at near nadir-incidence in a real-aperture mode, i.e. in a geometry and mode similar to that of SKIM. The airborne radar KuROS was deployed to provide simultaneous measurements of the radar backscatter and Doppler velocity, in a side-looking configuration, with an horizontal resolution of about 5 to 10 m along the line of sight and integrated in the perpendicular direction over the real-aperture 3-dB footprint diameter (about 580 m). The KaRADOC system has a much narrower beam, with a circular footprint only 45 m in diameter.

The experiment took place in November 2018 off the French Atlantic coast, with sea states representative of the open ocean and a well known tide-dominated current regime. The data set is analyzed to explore the contribution of non-geophysical velocities to the measurement and how the geophysical part of the measured velocity combines wave-resolved and wave-averaged scales. We find that the measured Doppler velocity contains a characteristic wave phase speed, called here C_0 that is analogous to the Bragg phase speed of coastal High Frequency radars that use a grazing measurement geometry, with little variations Δ_C associated to changes in sea state.

The Ka-band measurements at an incidence of 12° are 10% lower than the theoretical estimate $C_0 \simeq 2.4$ m/s for typical oceanic conditions defined by a wind speed of 7 m/s and a significant wave height of 2 m. For Ku-band the measured data is

https://doi.org/10.5194/os-2019-77
Preprint. Discussion started: 27 August 2019

Ocean Science
Discussions
Open Access
EGU

30% lower than the theoretical estimate 2.8 m/s. Δ_C is of the order of 0.2 m/s for a 1 m change in wave height, and cannot be confused with a 1 m/s change in tidal current. The actual measurement of the current velocity from an aircraft at 4 to 18° incidence angle is, however, made difficult by uncertainties on the measurement geometry, which are much reduced in satellite measurements.

1 Introduction

The total ocean surface current velocity (TSCV), is defined as the Lagrangian mean velocity right at the sea surface, corresponding to an effective mass transport velocity at the surface. The TSCV is only reliably measured by High-Frequency (HF) radars, available in some coastal regions. Elsewhere, its estimates depend on numerical models outputs, sea level and wind measurements using assumptions such as a balance between surface pressure gradient and the Coriolis force. Similar weaknesses affect the estimates of directional wave statistics. Such estimates of the TSCV and wave spectrum are not reliable at small scales, particularly so in the tropical ocean. (e.g. Sudre et al., 2013; Stopa et al., 2016). This limits our understanding of fluxes of heat, freshwater, carbon, plastics, and the coastal impacts of sea states. Whereas new data on ocean waves is becoming available with the SWIM instrument on the China France Ocean Satellite (Hauser et al., 2017), the direct measurement of surface current has been limited to a few regions and a single component of the current vector (Chapron et al., 2005; Rouault et al., 2010; Hansen et al., 2011). Several concepts based on SAR interferometry (Romeiser et al., 2003; Buck, 2005) or Doppler scatterometry (Rodriguez, 2018; Chelton et al., 2019) have been proposed for satellite missions aimed at mapping ocean surface current vectors. Airborne demonstrators have also been developed in that context (Martin et al., 2018; Rodríguez et al., 2018), and are now becoming operational tools for oceanographic research.

Direct Doppler measurements contain a geophysical Doppler (U_{GD}) due to waves (U_{WD}) and currents (U_{CD}) and a non-geophysical Doppler (U_{NG}) due to the platform velocity and acquisition geometry. The platform velocity in space being of the order of 7 km/s for low Earth orbit it is critical to have an accurate estimation of the measurement geometry to correctly estimate this non-geophysical Doppler.

As reviewed by Ardhuin et al. (2019), two main satellite concepts have emerged. One is a kilometer-scale resolution instrument based on InSAR (Buck et al., 2011). For this type of instruments, global coverage is not feasible today due to power and downlink capacity constraints. The other, based on Doppler satellite scatterometry, allows for a global monitoring of mesoscale currents at lower, but still unprecedented resolution, including the associated divergence field and ageostrophic motions. In that second category, the proposition of a Sea surface KInematics Multiscale monitoring (SKIM) satellite mission is based on a SWIM-like conically scanning radar, with a Doppler processing that allows to measure the surface current vector by combining different viewing azimuths across the satellite swath (Ardhuin et al., 2018). SKIM is built around a Ka-band pulsed radar with a specific processing chain using the phase difference of consecutive pulse returns to measure the line-of sight velocity

https://doi.org/10.5194/os-2019-77
Preprint. Discussion started: 27 August 2019

of ocean surface targets, together with the more usual Normalized Radar backscattering Cross-Section (NRCS). Both NRCS and velocity are resolved in range. In azimuth the resolution is 6 km for Doppler and 300m using unfocused SAR processing for NRCS. The platform also carries a nadir altimeter, that is necessary for tracking the ocean surface and set the timing of radar pulses, but can be used for sea level, geostrophic currents, and other nadir altimetry applications. In summary SKIM is a microwave Doppler Wave and Current Scatterometer, and these capabilities to measure sea level and directional wave spectra are used to improve on the retrieval of the surface current vector.

SKIM is one of the two candidate missions for the European Space Agency (ESA) 9th Earth Explorer. As part of the detailed design and feasibility studies (phase A), ESA funded a dedicated measurement campaign, which was organized from November 21 to 27, 2018, off the French Atlantic coast, with sea states characteristic of the open ocean and a well known tide-dominated current regime that is monitored by a 12 MHz High-Frequency radar (Ardhuin et al., 2009). A range of in-situ instruments (surface current drifters, drifting and moored wave-measuring buoys), as well as two airborne Doppler radars operating in the Ku (KuROS) and Ka (KaRADOC) bands were operated. The campaign goals were to

- demonstrate how the non-geophysical Doppler $U_{\rm NG}$ can be estimated from the motion of the platform carrying the radar, the antenna pattern properties and the azimutal and incidence dependence of the radar cross section.
- further explore the contribution to $U_{\rm GD}$ of currents and waves contributions, respectively $U_{\rm CD}$ and $U_{\rm WD}$, and illustrate how $U_{\rm GD}$ can be split into these two contributions (Nouguier et al., 2018),

  $$U_{\rm GD} = U_{\rm CD} + U_{\rm WD}, \tag{1}$$

  where the wave Doppler velocity plays the same role as the Bragg velocity in High-Frequency radar measuremements (Stewart and Joy, 1974).
- validate the Radar Sensing Satellite Simulator (Nouguier, 2019) and its capability to adapt to airborne configurations.

As highlighted in Figure 1, an airborne system differs from a satellite by its viewing geometry, with a much smaller footprint and incidence angle variations at scales comparable to the wavelength of the dominant ocean waves. The other obvious difference is the stability of the platform and its velocity, 7 km/s for low Earth orbit, and around 120 m/s for the ATR-42 aircraft used here. As a result, the performance of the airborne system requires a detailed simulator to be transposed to a satellite system. Still, airborne campaigns are useful to test effects that also occur in orbit, but with different magnitudes. The principle of the pulse-pair measurements and the non-geophysical contributions are detailed in section 2 and Appendix A. Section 3 presents the set up of the campaign and the results of the airborne measurements are exposed in section 4. Results and implications for SKIM are then discussed in section 5. Conclusions and perspectives follow in section 6.

2 Radar Doppler measurements of ocean velocities: theory

Details of how the phase difference in pulse pairs is related to the relative motion of a target, in our case surface gravity waves, and the radar are given in Appendix A. In the end, the line of sight velocity $V_{\rm LOS}$, looking at incidence angle θ and azimuth

https://doi.org/10.5194/os-2019-77
Preprint. Discussion started: 27 August 2019

Ocean Science
Discussions
Open Access
EGU

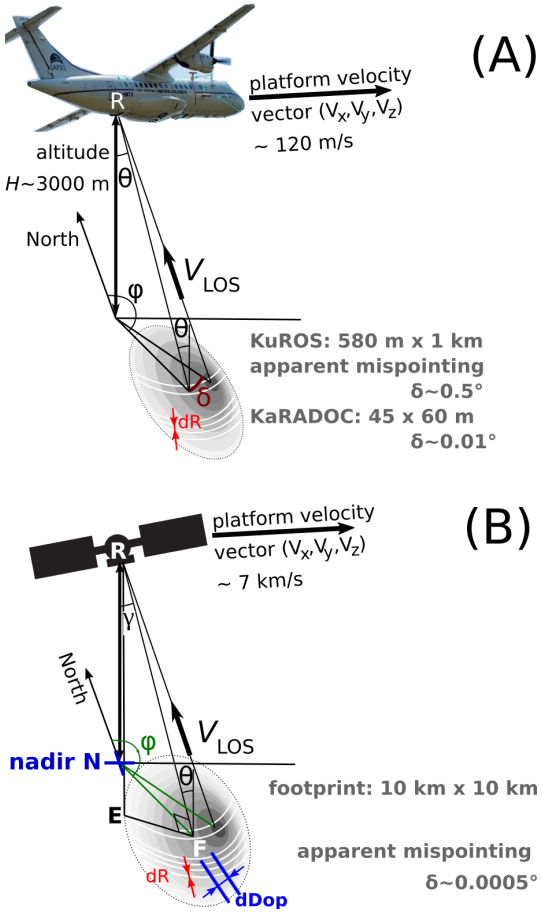

Figure 1. (A) Schematic of ATR-42 and KuROS instrument and definition of viewing angles, azimuth φ and incidence θ, and (B) comparison with the SKIM viewing geometry. A variation of surface backscatter across the footprint and as a function of azimuth φ is represented by the grey shading, and gives an effective mispointing δ. In KuROS data, each measurement is integrated in azimuth across the antenna lobe. In the case of SKIM, the use of unfocused SAR allows the separation of echoes in the azimuth direction with a resolution dDop$\simeq$ 300 m.

φ, is the sum of a horizontal geophysical Doppler velocity contribution $U_{\mathrm{GD}}(\varphi)$, and a non-geophysical velocity V_{NG}. The following measurement equation is given by projections of the target and sensor velocity vectors onto the line of sight as shown in figure 1,

$$U_{\mathrm{GD}}(\varphi) = \left[V_{\mathrm{LOS}}(\theta,\varphi) - V_{\mathrm{NG}}(\theta,\varphi)\right] / \sin\theta. \tag{2}$$

2.1 Non-geophysical velocity V_{NG}

In practice, V_{NG} is the radar velocity projected onto the effective look direction, that includes an apparent azimuth mispointing δ due to the finite antenna beamwidth combined with the variations of NRCS in the radar footprint. This NRCS variability

https://doi.org/10.5194/os-2019-77
Preprint. Discussion started: 27 August 2019

Ocean Science
Discussions
Open Access
EGU

includes both spatial gradients and azimuthal gradients. As a result, the beamwidth as a function of incidence is a very important parameter of the radar.

Table 1. KuROS and KaRADOC antenna radiation diagrams characteristics. All angles are in degrees. See Appendix B for the definitions of α and β

Instrument	KuROS	KaRADOC
Polarization	HH	HH
Azimuth 1-way beamwidth ($\alpha_{-3\mathrm{dB}}$)	15.0	1.85
Elevation 1-way beamwidth ($\beta_{-3\mathrm{dB}}$)	22.6	1.20
Boresight elevation (β^0)	11.8	12.1
Boresight azimuth (deg)	~ 0	-0.05

Table 1 summarizes the parameters of the KuROS and KaRADOC antennas. For KuROS they have been determined following the procedure detailed in Appendix B. For KaRADOC, they are the result of anechoic chamber measurements (Appendix C). As discussed in Appendix B, these parameters describe the antenna radiation diagrams when expressed as functions of variables, α and β, which do not coincide with azimuth and incidence. In the case of level flight and low incidence observations, one can however obtain a Gaussian approximation to the 1-way radiation diagram as:

$$G \simeq \exp\left(-\frac{\varphi^2}{2}\left[\frac{\sin^2(\theta)}{\sigma_\alpha^2}+\frac{(\beta_0-\tan(\theta))\tan(\theta)}{\sigma_\beta^2}\right]\right),$$

where $\sigma_\alpha = \alpha_{-3\mathrm{dB}}/\sqrt{8\log(2)}$, $\sigma_\beta = \beta_{-3\mathrm{dB}}/\sqrt{8\log(2)}$. For 12° observations the second term in the exponential can safely be neglected, and the effective azimuthal beamwidth can be estimated as:

$$\varphi_{-3\mathrm{dB}} = \frac{\alpha_{-3\mathrm{dB}}}{\sin(\theta)}.$$

When projected on the ground, $\varphi_{-3\mathrm{dB}}$ is thus larger than $\alpha_{-3\mathrm{dB}}$ by a factor $1/\sin(\theta)$, equal to 4.8 for 12° measurements. Provided that the beam does not grow too wide, the Gaussian approximation eq. (A27) of G as a function of φ can thus be used, with parameter

$$\sigma_\varphi \simeq \alpha_{-3\mathrm{dB}}/\left[\sin\theta\sqrt{8\log(2)}\right]. \tag{3}$$

When the sea surface NRCS is variable, this finite radar aperture gives an apparent mispointing that is the difference between the apparent azimuth φ_a and boresight azimuth φ_b, as detailed in Appendix A

$$\delta = \varphi_a - \varphi_b = \frac{1}{2}\frac{\sigma_\alpha^2}{\sin^2\theta}\frac{1}{\sigma^0}\frac{\partial\sigma^0}{\partial\varphi}. \tag{4}$$

If not corrected for, this apparent mispointing gives a spurious velocity that is the projection of the platform velocity onto the apparent line of sight

$$U_{\mathrm{AGD}} = \delta\sin\theta\sin\varphi_b V_p. \tag{5}$$

https://doi.org/10.5194/os-2019-77
Preprint. Discussion started: 27 August 2019

where V_p is the along-track velocity of the platform carrying the radar in the frame of reference of the solid Earth.

For our experimental KuROS configuration $\sigma_\alpha \simeq 6.36° = 0.11$ rad at $\theta = 12°$. As shown in section 3, $\partial_\varphi \sigma^0/\sigma^0$ is of the order of 0.10 rad^{-1} for a uniform wind speed of 11 m/s. This gives an apparent mispointing of the order of $\delta = 0.8° = 14 \times 10^{-3}$ rad, which would correspond to a 1.7 m/s error on U_{GD}. Here, it is important to note that KuROS was not specifically designed for this experiment, but primarily as a Calibration/Validation instrument for the CFOSAT mission, which required a broad radiation diagram. Though the analysis of the KuROS data helped uncover many interesting effects relevant to Doppler observations of the sea surface (for instance on the speckle noise dependence on observation direction) its design was not fully appropriate to validate the inversion of the geophysical velocities, for which the pencil-beam antenna diagram of KaRADOC was better suited.

As detailed in Appendix A, eq. (4) only applies for a narrow beam when projected on the ground, which is not a very good approximation for the KuROS case, even at an incidence of 12°. As shown in figure 2, the Gaussian approximation for the antenna pattern as a function of φ gives a too narrow distribution and does not take properly into account the azimuthal integration, leading to an overestimation of U_{AGD}.

As an example, figure 2 shows the variations of the two-way antenna radiation diagram G^2, of its Gaussian approximation, and of the $G^2\widetilde{\sigma^0}$ product as a function of azimuth at 12° incidence, for a northward-looking KuROS antenna ($\varphi_b = 0°$), using σ^0 data from the Drift4SKIM campaign on 22 November 2018, with a wind speed of 11 $\mathrm{m.s}^{-1}$ from azimuth 140°. The effect of the wind-induced azimuthal gradient of σ^0 is to shift the effective radiation pattern towards the brighter upwind/downwind directions, with an apparent pointing azimuth φ_a. The shift induced in this case is $\delta = \varphi_a - \varphi_b = -0.81° = -15 \times 10^{-3}$rad, a very large number compared to the 85 microradians pointing accuracy required to meet the 1 cm/s horizontal current accuracy goal.

Figure 3.A shows a typical azimuthal variation of $\widetilde{\sigma^0}$ for an incidence of 12° using a Ku-band radar. As expected for near-nadir measurements (Chapron et al., 2002; Munk, 2008), the NRCS is largest in the downwind look direction ($\varphi = -40°$), has a secondary peak in the upwind direction, and is weakest in the crosswind look directions. Figure 3.B shows the expected spurious contribution U_{AGD} to the geophysical velocity U_{GD}, if the apparent mispointing δ is not corrected for. This uses an aircraft velocity $V_p = 120$ m s^{-1}, for the KuROS and KaRADOC cases. The Ku-band NRCS fit has been used for the Ka-band instrument as well. This is a reasonable assumption for order-of-magnitude estimates.

Because both the azimuth gradient Doppler U_{AGD} and the spatial gradient Doppler U_{SGD} are proportional to $V_p\sigma_\varphi^2$ it is clear that the broad KuROS antenna pattern requires a very accurate estimation to correct for U_{AGD}, which is almost negligible for KaRADOC or DopplerScatt (Rodríguez et al., 2018), thanks to their narrow azimuthal beam aperture. Another remark is that the approximate expression eq. (A35), though it gives the appropriate dependency of U_{AGD} with respect to look azimuth, tends to over-predict its magnitude, as the widening associated to the ground projection saturates for broad beams.

At small scales, spatial gradients add to the azimuthal gradient and also induce a spurious velocity with the same expression as a function of $\widetilde{\sigma^0}$. Using the simple case of a single Fourier component $\widetilde{\sigma^0} = \varepsilon \sin[\nu(\varphi - \varphi_b)]$ allows one to evaluate the

https://doi.org/10.5194/os-2019-77
Preprint. Discussion started: 27 August 2019

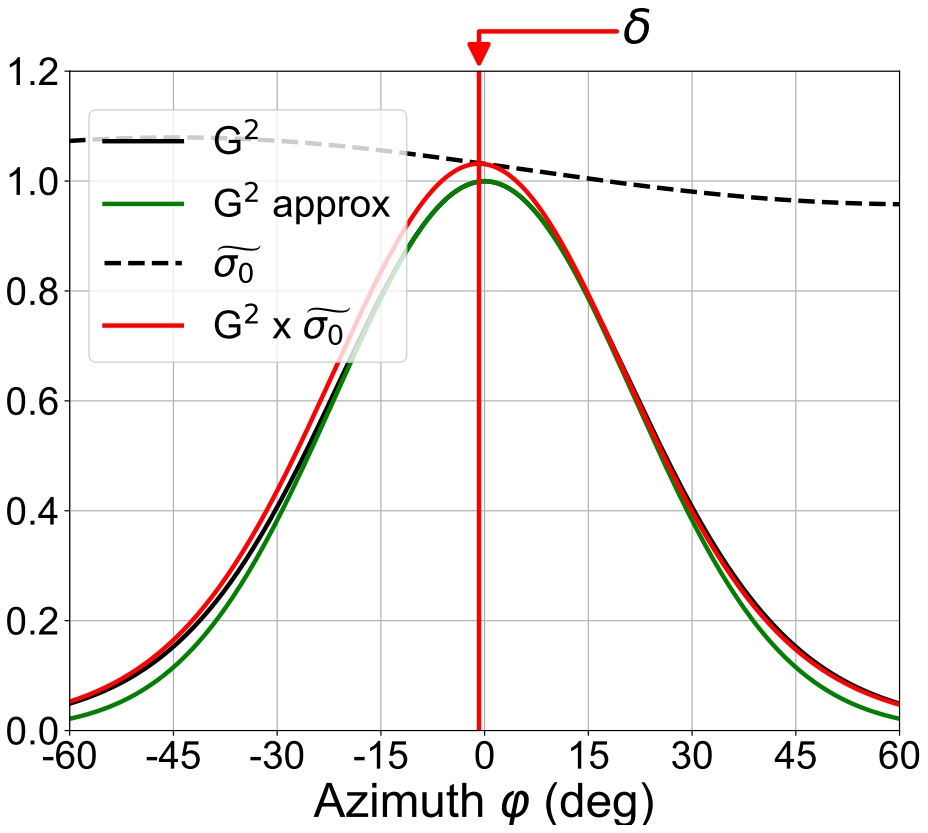

Figure 2. KuROS azimuth integral weight at $\theta = 12°$, north-facing antenna (black), Gaussian approximation (eq. A27) (green) and variation of $\widetilde{\sigma^0}$ for a typical 11 $\mathrm{m.s^{-1}}$ wind from 140° (dashed black). The peak of the $\widetilde{\sigma^0}\ G^2$ product (red) is shifted with respect to the peak of G^2 by $\delta \simeq -0.81°$.

importance of different scales. The azimuthal shift can be obtained as

$$\delta = \varepsilon \exp\left(-\frac{(\nu^2+1)\sigma_\varphi^2}{4}\right) \sinh\left(\frac{\nu\sigma_\varphi^2}{2}\right). \tag{6}$$

In the slow-variation limit $\nu, \sigma_\varphi \to 0$, and eq. (6) this expression coincides with eq. (A30). For faster variations, one sees that the largest disturbance is obtained when $\nu \sim \sqrt{2}/\sigma_\varphi$. This azimuthal wavenumber is such that the footprint can host a bright and a dark patch, one on either side of the look direction. This configuration creates the largest disturbance for a given value of the brightness contrast ε. δ in this case is given by

$$\delta_{\max} = \varepsilon\sigma_\varphi \mathrm{e}^{-1/2}/\sqrt{2}. \tag{7}$$

https://doi.org/10.5194/os-2019-77
Preprint. Discussion started: 27 August 2019

Ocean Science
Discussions
Open Access
EGU

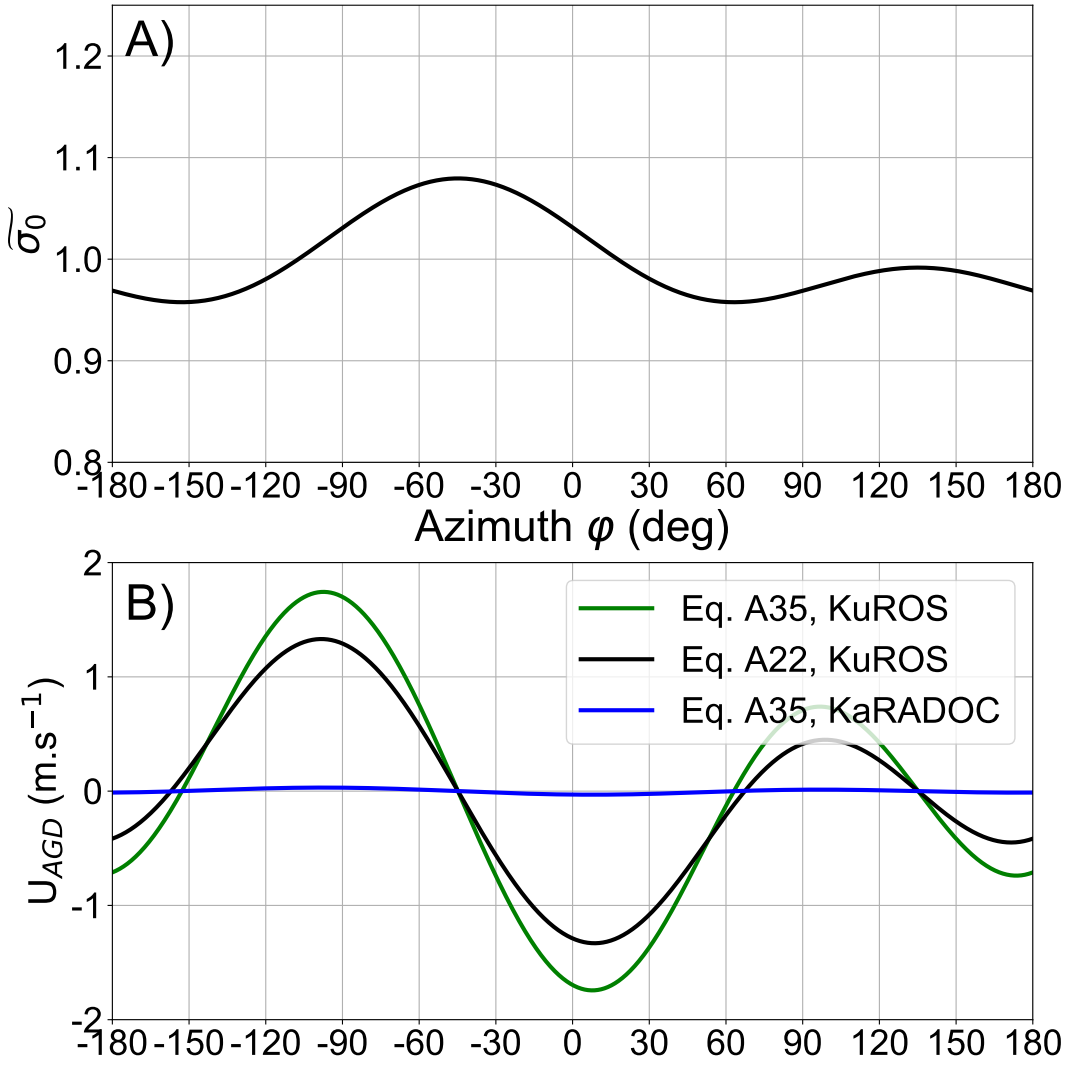

Figure 3. A) Example of azimuthal variation of $\widetilde{\sigma^0}$ at 12 ° incidence, corresponding to the November 22 case (11 m/s wind from 140 °) discussed in section 3, and B) associated spurious velocity U_{AGD} as a function of look azimuth φ_b in the case of a port-looking antenna mounted on a platform in level flight at 120 m/s. For the KuROS case, green lines show the result of the approximate eq. (A35) and black lines show the result of the full azimuthal integration eq. (A22). The blue line represents the result of eq. (A35) for the KaRADOC, using the same $\widetilde{\sigma^0}$ as in the Ku-band case.

Although the relative variations $\partial\sigma^0(\varphi)/\partial\varphi/\sigma^0$ are larger for larger incidence angles, this is more than compensated by the $1/\sin^2\theta$ reduction in azimuthal diversity across the footprint. This is why this effect can be neglected for much higher incidence angles (Rodríguez et al., 2018).

https://doi.org/10.5194/os-2019-77
Preprint. Discussion started: 27 August 2019

2.2 Geophysical velocity U_{GD}: Waves and Current Doppler

The geophysical part of the Doppler shift measured by a microwave radar over the ocean, using both Along-Track-Interferometry and Doppler centroid techniques is caused by the backscatter-weighted average of the surface velocities along the line of sight, as illustrated in figure 4.

For a perfect sine wave of period T propagating over deep water, the phase speed of the wave is

$$C = \frac{gT}{2\pi} + U\cos(\varphi_w - \varphi_U) \tag{8}$$

where U is the current speed, φ_w is the wave propagation azimuth direction, and φ_U is the current direction. Measuring the phase speed deviation from the theoretical value is the principle of the coastal HF radars (Barrick et al., 1974; Stewart and Joy, 1974), for which the grazing angles coherent Bragg back-scattering mechanism selects very effectively the sine wave components of the sea state which interact with the radio waves.

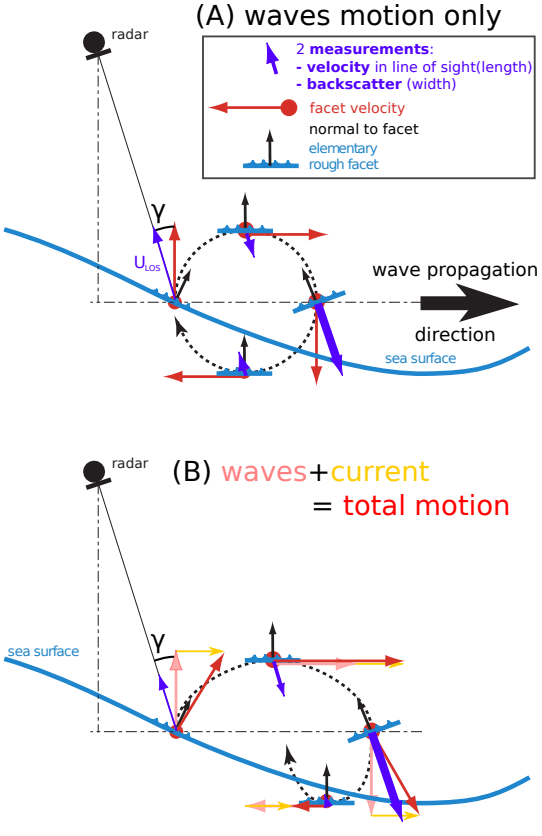

Figure 4. Schematic of (A) wave and (B) wave and current contributions to Doppler velocities at the scale of elementary facets. These are averaged into a radar pixel, so that sub-pixel waves contribute a mean velocity due to the correlation of surface slopes and velocities in the wave field.

https://doi.org/10.5194/os-2019-77
Preprint. Discussion started: 27 August 2019


Ocean Science
Discussions
Open Access
EGU

In the case of KuROS, SKIM, or other systems for which the backscattering mechanism is not selective, a superposition of waves contributes. We get a compound mixture of C's, and the different terms become (Nouguier et al., 2018; Yurovsky et al., 2019),

$$C \rightarrow U_{\mathrm{GD}} \tag{9}$$

$$\frac{gT}{2\pi} \rightarrow U_{\mathrm{WD}} \tag{10}$$

$$U \rightarrow U_{\mathrm{CD}} \tag{11}$$

where the current U sampled at depth $k/4\pi$ (Stewart and Joy, 1974) for a monochromatic sine wave, is now U_{CD}, a weighted average of the currents at different depths, where the weighting function is determined by the wave slope spectrum. Indeed, the velocity U_{GD} integrates the velocity of the tilted-facets on the ocean surface. Within facets, quasi-specular and specular points are selected, further modulated by the local directional tilts $\nabla\eta$, leading to a modulated averaged intensity and a weighted velocity as

$$\sigma^0 = \int \sigma(\nabla\eta) P(\nabla\eta) d\nabla\eta \tag{12}$$

$$\sigma^0 * V_{LOS} = \int V_{LOS}(\nabla\eta)\sigma(\nabla\eta) P(\nabla\eta) d\nabla\eta \tag{13}$$

with $\sigma(\nabla\eta)$ an individual local radar cross section, corresponding to a tilted facet, with a local line-of-sight velocity V_{LOS}, and $P(\nabla\eta)$ the facet-tilt probability distribution.

As the incidence angle is increased beyond 25°, the backscatter is dominated by Bragg scattering and the phase speeds that contribute are the Doppler-shifted Bragg waves (Rodríguez et al., 2018). In our case, Bragg scattering is generally negligible except for the lowest wind speeds, and the Ka-band resonant Bragg scattering scale at 12° is about 2 cm, around the capillary-gravity wave transition, corresponding to the minimum phase velocity of about 23 cm/s. A general analysis valid for all incidence angles is presented by Yurovsky et al. (2019). Here we focus on incidence angles from 4 to 20° where the backscatter modulation is dominated by tilt effects (Kudryavtsev et al., 2017).

The correlation of surface slope and line-of-sight velocity defines the mean slope velocity in direction φ, msv(φ) (Nouguier et al., 2018). For linear ocean waves, this equals the correlation of vertical velocity gradients and displacements, equal to half the Stokes drift in direction φ, $U_S \cos(\varphi - \varphi_S)$. The surface Stokes drift magnitude U_S and direction φ_S can be computed from wave buoy measurements (Kenyon, 1969; Ardhuin et al., 2009). Even though U_S is highly correlated with the wind speed, with a Pearson's linear correlation coefficient of 0.85 or so, it has a strong variability with the sea state as illustrated in Fig. 5.a.

Using a Kirchoff approximation, the variation of wave Doppler with observation direction φ can be computed from the wave spectrum (eq. 16 in Nouguier et al., 2018, see also Appendix C),

$$U_{\mathrm{WD}}(\varphi) = G_D U_S \cos(\varphi - \varphi_{\mathrm{WD}}) \tag{14}$$

where U_S is the magnitude of the surface Stokes drift vector, which has a direction φ_S, and the direction φ_{WD} is found to be within a few degrees of φ_S. The Doppler imaging factor G_D is a weakly varying function of the radar frequency and incidence

https://doi.org/10.5194/os-2019-77
Preprint. Discussion started: 27 August 2019

angle, but also of sea state (Nouguier et al., 2018)

$$G_D = \frac{-1}{2\sigma^0 \cos^4\theta \tan\theta} \frac{\partial \cos^4\theta \sigma^0}{\partial \tan\theta}. \tag{15}$$

For Ka-band, we may use a typical variation of σ^0 of the form, (Walsh et al., 2008; Nouguier et al., 2018),

$$\sigma^0 \simeq \frac{\sigma^0_{\max}}{\cos^4\theta} \exp[-A\tan^2\theta + B\tan^4\theta] F(\varphi) \tag{16}$$

where non-Gaussian corrections are, $B \simeq 0.5676 A^{1.332}$ and the modification of $\sigma^0_{\max}$ related to the $\mathrm{mss}_{\mathrm{shape}}$ of Nouguier et al. (2016), and $A = 1/\mathrm{mss}_{\mathrm{shape}}$

$$G_D \simeq \frac{2A\tan\theta - 4B\tan^3\theta}{2\tan\theta} \simeq \frac{1 - 1.1\mathrm{mss}^{-0.33}_{\mathrm{shape}} \tan^2\theta}{\mathrm{mss}_{\mathrm{shape}}}. \tag{17}$$

For Ku-band the $\mathrm{mss}_{\mathrm{shape}}$ is generally smaller than the Ka-band value, in particular for wind speeds over 5 m/s, as shown in 5.b.

Average values of the $\mathrm{mss}_{\mathrm{shape}}$ give typical values $G_D \simeq 25$, slowly decreasing with increasing θ. Therefore, both Stokes drift magnitude and G_D grow with wind speed. It may thus be more practical to express U_{WD} in the following form

$$U_{\mathrm{WD}}(\varphi) = M_{\mathrm{WD}} \cos(\varphi - \varphi_{\mathrm{WD}}) \tag{18}$$

$$= (C_0 + \Delta_C) \cos(\varphi - \varphi_{\mathrm{S}} - \delta_\varphi) \tag{19}$$

where M_{WD} varies very little for most of the sea state conditions, around $C_0 = 2.2$ m/s in Ka-band and $C_0 = 2.4$ m/s in Ku band. In other words, most of the variability of U_{WD} is controlled by the directionality effect and the magnitude M_{WD} is a weakly varying function of the wave age and presence of swell (see also Yurovsky et al., 2019; LOPS, 2019).

3 Campaign overview

3.1 Organization of the campaign

Given our objectives of demonstrating the sensitivity of airborne Doppler measurements to the geophysical contributions of currents and waves, it was important to have commonly accepted reference measurements for these parameters. Also, in order to verify the limited effect of wave development on the geophysical Doppler velocity U_{GD}, we decided to go to an oceanic environment, open to offshore swells, which makes our experiment different from previous Doppler airborne campaigns (Martin et al., 2016; Rodríguez et al., 2018).

Field work was focused in two "boxes" (Figure 6) named the "offshore box", around the "Trefle" buoy (see below), and the "Keller race box" to the north of the Ushant island. Both boxes are in the range of coverage of a WERA-type High-Frequency radar (Gurgel et al., 1999; Gurgel and Barbin, 2008), operated by Service Hydrographique et Oceanographique de la Marine (Shom) and already used for several studies, in particular related to wave-current interactions (Ardhuin et al., 2009, 2012; Guimaraes et al., 2018). The "Keller race box" is an area with very strong horizontal gradients of the current. Although it is

https://doi.org/10.5194/os-2019-77
Preprint. Discussion started: 27 August 2019

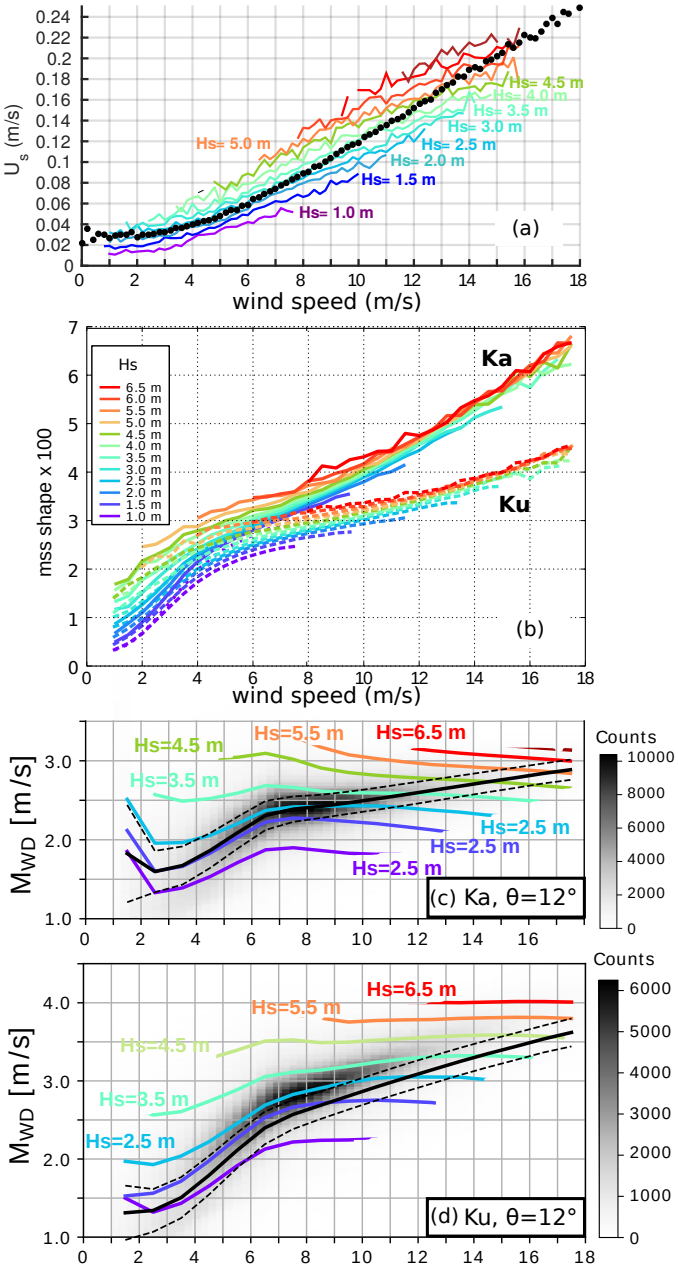

Figure 5. Computed variability of the wave slope velocity, the mss and the Doppler magnitude M_{WD} that is close to the ratio of these two quantities. M_{WD} was computed for a wide range of modeled ocean wave spectra, plotted here as a function of the wind speed. The colored curves show the median value for different classes of wave height for a given wind speed, each curve is separated by 0.5 m in (a) and (b) or 1 m in (c) and (d).

https://doi.org/10.5194/os-2019-77
Preprint. Discussion started: 27 August 2019

easy to show a strong effect of the current on a measured Doppler, the spatial variability of the sea state is difficult to measure in situ, introducing uncertainties when combining $U_{\mathrm{CD}} + U_{\mathrm{WD}}$ in a forward model or using U_{WD} estimates when retrieving U_{CD} from the measured U_{GD}.

The "offshore box", on the other hand, was chosen for its spatial uniformity, being located far enough from the islands and with a near-uniform depth of 110 m. Only airborne data acquired over the "offshore box" are presented in this paper.

The week around spring tides of November 2018 was targeted, in order to allow for a wide range of current speeds (Fig. 7a), as well as to accommodate plane availability constraints.

Ground truth measurements comprised two permanent operational systems: the 12 MHz WERA-type HF radar mentioned previously, with expected depth of measurement around 1 m (Stewart and Joy, 1974), and a wave-measuring buoy 'Pierres Noires', also known by its World Meteorological Organization number 62069.

Dedicated instrumentation was also deployed for the campaign:

–the "Trefle" buoy was moored at 5°25' W, 48°25' N, in the middle of the offshore box. This buoy monitored the surface motion (Sutherland et al., 2016) and provided directional wave spectra (Fig. 8).

– two types of drifters including CARTHE drifters (Novelli et al., 2017), drogued around 40 cm, and SVP drifters (Niiler and Paduan, 1995), drogued at 15 m, were deployed in the measurement areas.

– the R/V Thalia worked in the offshore box, provided continuous underway measurements of meteorological parameters using a Météo-France "BATOS" operational system comprising a Vaisala WXT-series sonic anemometer located approximately 10 m above sea surface. The ship also carries a SBE21 thermosalinograph.

In the summer, the so-called "Ushant tidal front" (Le Boyer et al., 2009) has a strong influence on the current and conditions in the offshore box. CTD casts were performed from R/V Thalia during the campaign, that showed the water column to be very well mixed, surface-to-bottom potential density anomalies being smaller than $0.002\ \mathrm{kg.m^{-3}}$. The spatial homogeneity was also checked using the ship thermosalinograph and an infrared camera mounted on a second plane (a Piper PA-23 also operated by SAFIRE) which surveyed the offshore box in a "lawn mowing" pattern, flying under the clouds from an altitude of 500 m to 1000 m. Interesting small-scale surface signatures could be observed on calm days, but it is clear that no density-associated mesoscale structure was present.

The aircraft measurement geometry over the "offshore box" consists of relatively long (12 km) and straight tracks with different aircraft headings, forming a star pattern, with examples shown in Figures 6. Regarding the radar instruments, KaRADOC had its antenna fixed relative to the aircraft and looking to port, while the KuROS antenna could either be fixed in the up-track or port cross-track directions, or rotate in the clock-wise sense relative to the flight line. Only the port-looking Doppler KuROS data are presented in this paper. Tracks heading was every 12, 22.5 or 45° in azimuth φ, depending on flight duration constraints.

3.2 Geophysical conditions

A wide range of geophysical conditions were encountered during the one-week long campaign. The aircraft flew four times over the "offshore box": on 11/21 from 13:50 to 15:50, on 11/22 from 12:15 to 15:00, on 11/24 from 11:20 to 13:20, and finally

https://doi.org/10.5194/os-2019-77
Preprint. Discussion started: 27 August 2019

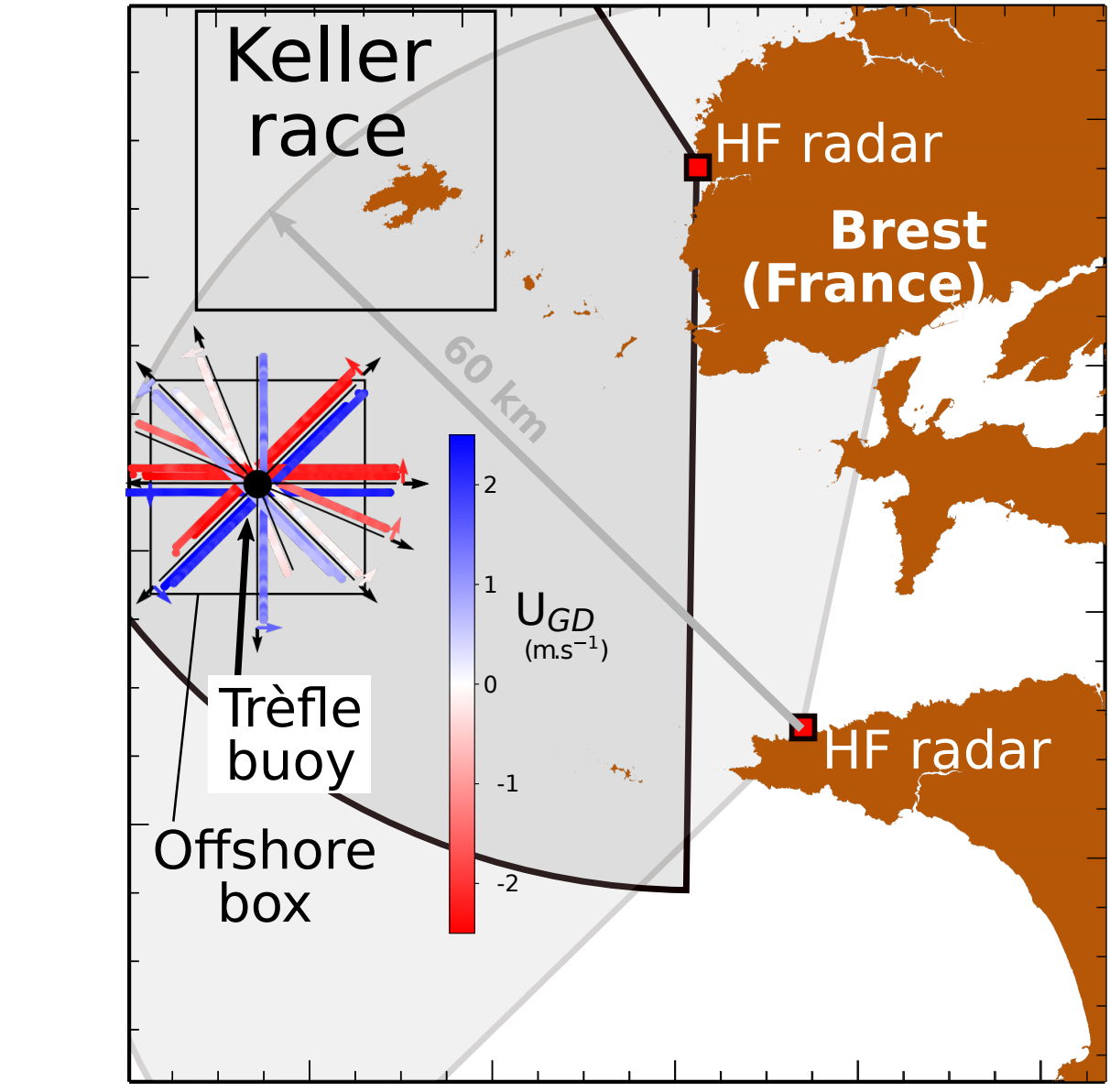

Figure 6. Location of measurement campaign and in situ assets, including a map of KaRADOC measurements of the Doppler velocity acquired on 22 November 2019.

on 11/26 from 09:40 to 11:00. In this paper, we focus on data acquired on 11/22 and 11/24 as the geophysical conditions were interesting and complementary (see below) and data were acquired with the largest azimuth diversity on these two days.

The November 22 flight took place at the end of an interesting steady southeasterly wind episode (13 m/s from 140°). The November 24 flight in contrast took place during a steady weak south-westerly wind period (5 m/s from 270°) (Fig. 7b).

https://doi.org/10.5194/os-2019-77
Preprint. Discussion started: 27 August 2019

Ocean Science
Discussions
Open Access
EGU

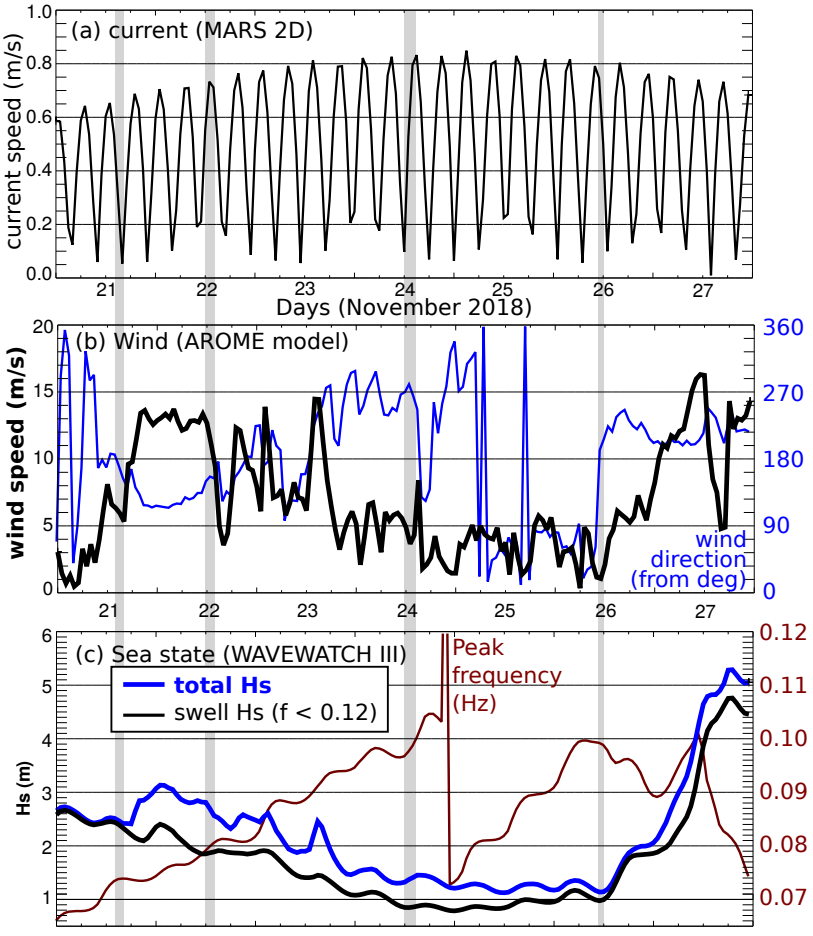

Figure 7. Time series at the location of the Trefle buoy (5°15' W, 48°25' N) in the offshore box of (a) ocean surface current speed output from the numerical model MARS2D (Lazure and Dumas, 2008); (b) wind speed (black) and direction (blue) from the regional operational model of MeteoFrance, AROME and (c) Total (blue) and swell (black) significant wave height and wave peak frequency (red) from the numerical wave model WAVEWATCH III run at LOPS (Roland and Ardhuin, 2014). The four time frames shaded in grey correspond to the times of KuROS measurements with fixed antenna, with observed environmental parameters detailed in table 2.

The wave height during the campaign was dominated by the presence of two swell systems from North Atlantic remote storms. The swell height decreased from 2.5 to 0.9 m from the 21 to 24 November, with a peak frequency increasing from 0.07 Hz to 0.1 Hz, and a mean direction gradually veering from west to north-west. This swell contributes little to the Stokes drift (about 10% of the windsea contribution on 22/11).

The main environmental conditions at the time of these star-pattern flights with a fixed antenna are summarized in Table 2.

https://doi.org/10.5194/os-2019-77
Preprint. Discussion started: 27 August 2019

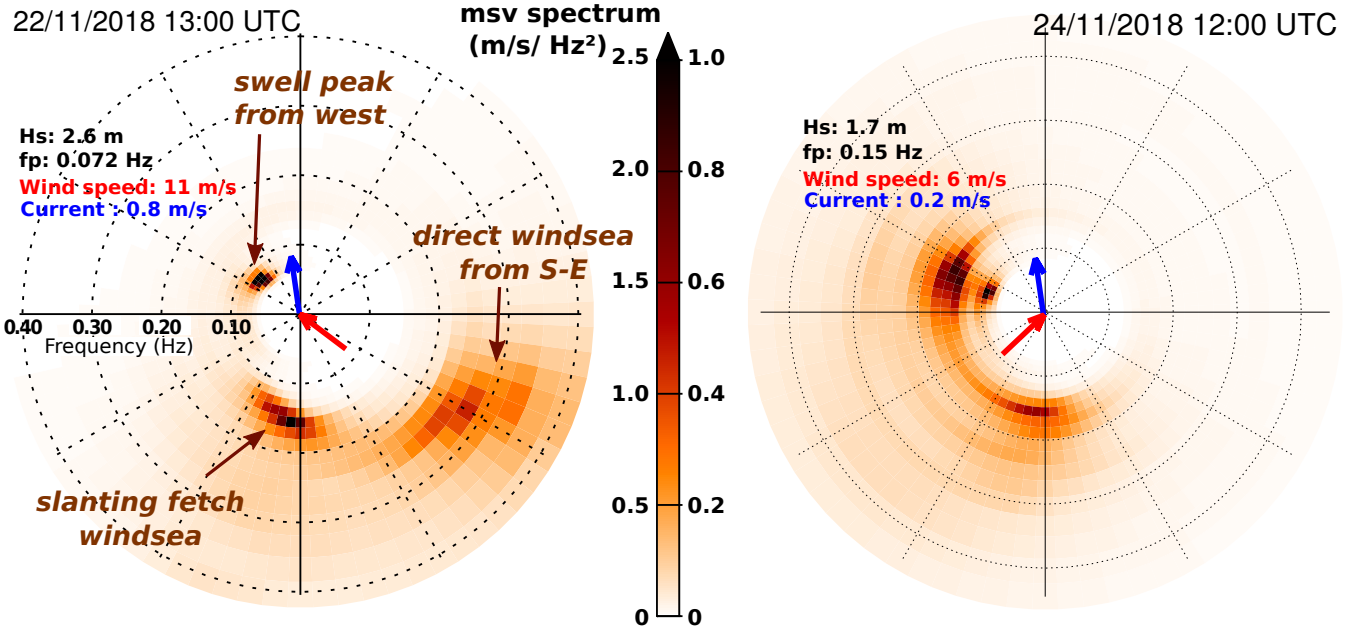

Figure 8. Directional wave spectra $E(f_r, \theta)$, where f_r is the relative wave frequency and θ is the azimuth winds are coming from, estimated from the buoy motions of Trefle on 22/11 at 13:00 UTC and Spotter buoy number 10 on 24/11 at 12:00 UTC. The measured directional moments were transformed with the Maximum Entropy Method (Lygre and Krogstad, 1986), and Doppler shifted with $f_r = f - \mathbf{k} \cdot \mathbf{U}/(2\pi)$ for the moored Trefle buoy.

3.3 KuROS set-up

KuROS is a Ku-Band (13.5 GHz) pulse pair Doppler radar with a dual antennae system and azimuthal scanning possibility, which was developed in the framework of the CFOSAT pre-launch studies. Of the two antennas, the Low Incidence antenna is nominally centered on 14° incidence, while the Medium Incidence antenna is nominally centered on 40° incidence. Only the LI antenna, which was the more relevant for SKIM, was used during the campaign. This antenna uses a HH polarization. A comprehensive description of the system can be found in Caudal et al. (2014), with an important modification consisting of a new antenna with characteristics given in Table 1.

The radar transmits a frequency-modulated pulse (chirp) with a 100 MHz frequency band, achieving a 1.5 m range resolution and an effective resolution around 7 m in elevation once projected on the ground (at 12°). The 1-way 3-dB footprint in azimuth is 580 m wide at 12° and 3000 m flight altitude. The Pulse Repetition Frequency (PRF=1/PRI) depends on the altitude, and is 23 kHz when the aircraft flies at 3000 m. The ambiguity on the Doppler velocity measurement (see section A2.1 in the appendices) is about 126 m/s, which is much larger than expected from the measurements (below aircraft speed of 120 m/s).

As discussed in Appendix A, accuracy requirements on observation geometry are much less stringent for cross-track than for up/down-track Doppler observations. The Doppler data discussed in this article were all collected with the KuROS antenna in the port-looking orientation. This configuration also ensures an overlap with the KaRADOC footprint.

https://doi.org/10.5194/os-2019-77
Preprint. Discussion started: 27 August 2019

Ocean Science
Discussions
Open Access
EGU

Table 2. Velocities of current and Stokes drift measured or estimated near position 48.25 N, 5.25W, in cm/s, and wind vector in m/s. Please note that the Stokes drift is only integrated up to 0.5 Hz. Buoy data correspond to the Trefle buoy for 22/11 and Spotter buoy number 10 for 24/11.

Time	CARTHE	SVP	HF-radar	buoy (U_s, V_s)	WW3 (U_s, V_s)	wind (ship)	wind (Arome)
21/11 14:00	(21,73)	(21,72)	(15,71)	(0.69, 2.23)	(0.44,2.06)	(-3.3,8.0)	(0.5,6.3)
21/11 14:30	(17,59)	(19,58)	(16,60)	(0.88, 2.02)		(-2.3,6.8)	-
21/11 15:00	(15,45)	(16,49)	(12,39)	(0.21 2.54)	(0.41,2.12)	(-4.4,5.2)	(-1.1,5.8)
21/11 15:30	(14,30)	(15,21)	(11,31)	(0.23, 1.97)		(-4.7,8.2)	-
22/11 12:00	(-5,107)	(-3,81)	(-14,58)	(-5.47,8.86)	(-7.38,11.55)	(-8.9,6.8)	(-6.8,10.7)
22/11 12:30	(-1,133)	(4,84)	(-7,74)	(-5.44,9.19)	(-7.42,11.37)	(-9.4,7.2)	-
22/11 13:00	(3,97)	(4,94)	(-5,89)	(-4.72,8.37)	(-7.07,11.39)	(-8.5,7.9)	(-5.2,10.0)
22/11 13:30	(8,97)	(12,89)	(3,91)	(-4.75,8.02)	(-6.68,11.50)	(-4.4,9.2)	-
22/11 14:00	(12,94)	(12,87)	(11,78)	(-3.28,7.19)	(-6.35,11.66)	(-3.6,11.5)	(-4.4,8.3)
22/11 14:30	(11,87)	(11,78)	(14,73)	(-3.35,6.93)	(-5.82,11.76)	(-7.2,8.0)	-
24/11 11:30	(-8,-6)	(-11,-6)	-	(2.47,1.81)	-	(5.0,2.7)	-
24/11 12:00	(0,20)	(-7,16)	-	(2.49,1.20)	(0.75,2.92)	(4.0,3.9)	(4.9,0.1)
24/11 12:30	(1,44)	(-1,40)	-	(2.92,1.66)	(0.68,2.71)	(4.7,2.8)	-
24/11 13:00	(6,64)	(1,59)	-	(3.20,1.35)	(0.68,2.71)	(4.8,2.6)	(3.5,-0.7)
24/11 13:30	(8,82)	(2,78)	-	(2.73,1.29)	(0.70,2.60)	(3.3,2.8)	-
26/11 10:00	(-18,-86)	(-20,-87)	(-11,-71)	(0.46,-0.19)	(0.59,-0.64)	(-2.9,0.7)	(-1.0,-0.6)
26/11 10:30	(-23,-82)	(-24,-84)	(-19,-71)	(0.32,-0.23)	(0.59,-0.64)	(-0.7,1.4)	-
26/11 11:00	(-25,-73)	(-27,-74)	(-22,-77)	(0.30,-0.20)	(0.59,-0.64)	(0.6,1.4)	(0.2,1.1)

3.4 KaRADOC sensor

The Ka-band RADar for Ocean Current monitoring (KaRADOC) airborne radar sensor has been developed for the DRIFT4SKIM campaign. KaRADOC is derived from the Still WAter Low Incidence Scattering (SWALIS) instrument, developed for the measurement of the NRCS of inland water surfaces in Ka-band. Further details on the system are given in Appendix C.

KaRADOC was mounted under the ATR42 aircraft, in a port-looking configuration. The two-way 3 dB footprint from 3000 m altitude over a flat sea surface is an ellipse with diameters 45 and 60 m in the cross-track and along-track directions, respectively. The incidence is selected by varying the working frequency. Data was acquired at different incidence angles, from 6 to 14°, corresponding to a change of frequency from 32.5 to 38.2 GHz. Here we only report on $\theta = 12°$ observations.

This radar does not incorporate a range-resolution scheme: the transmitted pulses last several μs, and the whole FOV is illuminated simultaneously. The demodulated return signal is sampled at 15 MHz and archived. It is essentially constant while the electromagnetic wave is actually interacting with the sea surface. The useful signal segment is selected and its

https://doi.org/10.5194/os-2019-77
Preprint. Discussion started: 27 August 2019

average is computed in order to reduce the thermal noise contribution, yielding one complex amplitude for each pulse. Several hundred pulses are sent at 4 kHz PRF for each burst of measurements, with a burst repetition frequency of the order of 5 to 10 Hz, depending on the number of incidence angles in the scanning sequence. These parameters have been varied during the acquisitions. Though they have a strong impact on NRCS estimates quality and Doppler estimates noise, we have found the low-pass filtered Doppler signal to be robust.

The pulse pair complex signal is averaged for each burst, in order to reduce the effect of coherent speckle. One complex pulse-pair sample is thus obtained per burst. Even at the lowest burst repeat frequency of 5 Hz, the plane moves by less than a third of the FOV along-track extension between bursts.

4 Measurements

4.1 Qualitative description of the KuROS data

We will start with the σ^0 data because it is a more generally understood property of the sea surface and the analysis of its variation in azimuth φ and elevation θ is necessary to interpret the Doppler mean value and modulations. However, it is interesting to first look at the rawest available data, which can be displayed as images of backscatter and Doppler.

Figure 9 shows pieces of the first few tracks acquired on November 22, when the wind speed was around 11 m/s, after removing the aircraft velocity (see Appendix B and C for details).

The first remark is that the back-scatter, after correcting for an incidence-varying mean trend, is smooth with a typical amplitude of variation of 1 dB (Fig. 9.A). This smoothness comes from the large footprint and radiometric quality of the data. The KuROS data clearly reveals the presence of the swell from the west, with a peak frequency of 0.07 Hz corresponding to a wavelength $L = 320$ m. This is particularly visible in the north-south oriented flight tracks number 6 and 5 in Fig. 9.B and Fig. 9.E-F for a zoom on track 6. The apparent swell direction (dashed lines in figure 9.B) differs from its true direction due to scanning distortion (Walsh et al., 1989; Sutherland and Brozena, 2018), as the swell propagates during the measurement at a phase speed of 22 m/s, combined with an aircraft speed of 120 m/s.

Shorter waves, as measured by the TREFLE buoy (Fig. 8), occupy a wide range of directions from a narrow windsea peak from the south at 0.16 Hz ($L = 60$ m), to a broad directional distribution at 0.22 Hz ($L = 30$ m) with a mean direction of 130° and a half width (spread) of 45°, hence covering directions from 85° to 175°. These shorter components are present in data from flights tracks 5 and 6, in the form of very narrow stripes with orientations shown with the short dashed lines in 9.B and Fig. 9.E-F for a zoom on track 6. The "long-crested" appearance of short waves in (D) and (E) is an artefact of the wavefront-matching observation (Jackson et al., 1985), with all other directions averaged out by the large azimuth width of the radar beam. If purely geophysical, the velocity associated to the Doppler shifts is expected to give the wave propagation direction. For flight track 6 in (F) and (G), the long swell propagates towards the radar and the brighter slopes (white) correspond to eastward velocities toward the radar (blue). This will be discussed in further details below. Finally (H) and (I) exhibit chevron patterns with crests facing both north-east and nort-west directions, whereas the waves from the south-west are expected to be much longer than those from the south-east, which is not apparent in the KuROS data.

https://doi.org/10.5194/os-2019-77
Preprint. Discussion started: 27 August 2019

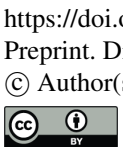

Ocean Science
Discussions
Open Access
EGU

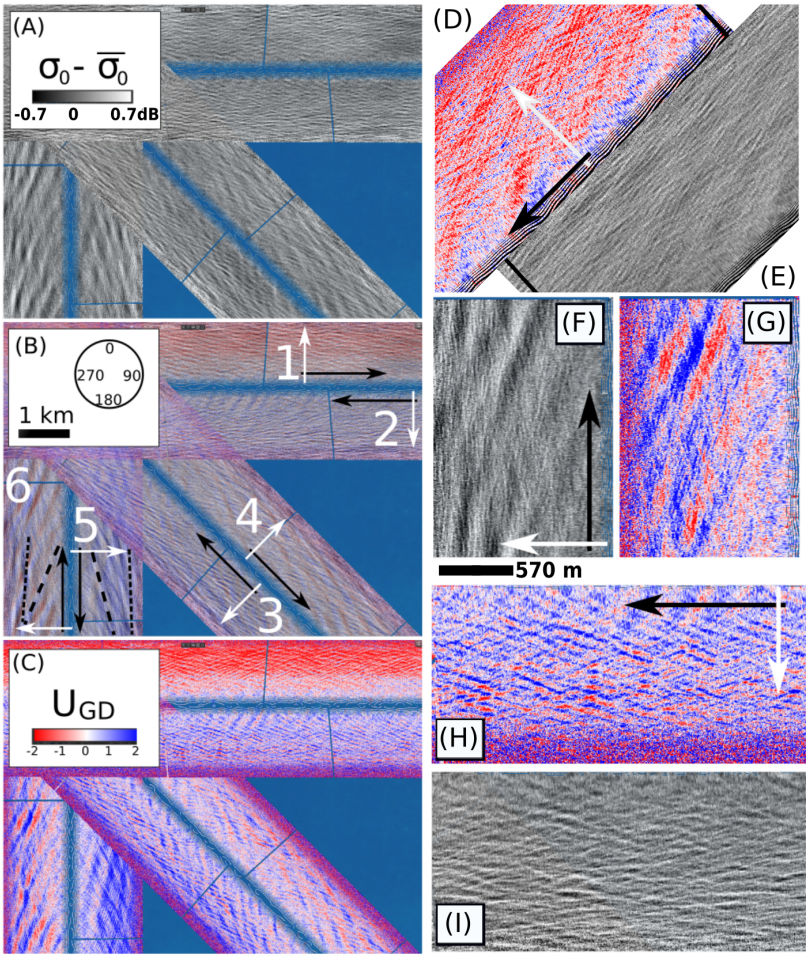

Figure 9. (A) and (C) Mosaic of radar intensity and Doppler acquired on November 22 with a fixed antenna relative to the aircraft, looking left. (B) overlay of the Doppler and intensity. Flight tracks are numbered 1 to 6, Black arrows indicate the flight direction and white arrow point into the radar look direction. The long dashed lines represent the apparent direction of swell crests. (D)-(E) are enlarged pieces of (A) and (C) for (D) and (E) a flight track that was now shown and (F)-(I) flight tracks 6 and 2. The 570 m scale bar applies to (E)-(H) and correspond to the 3-dB width of the radar beam at 12° incidence, i.e. near the middle of the swath.

4.2 Ku-band backscatter

Given the expected large influence of the wind, wave and current directions, and the high noise on the aircraft measurement geometry estimation, data have been averaged along 30-s track portions. Data have been averaged in incidence angle (across track) every 1° with one point every 30-s. As highlighted before, full tracks are straight and relatively long (12 km) in a homogeneous ocean region. Each track has a different aircraft heading, forming a "star" pattern, sampling a wide range of azimuths.

https://doi.org/10.5194/os-2019-77
Preprint. Discussion started: 27 August 2019

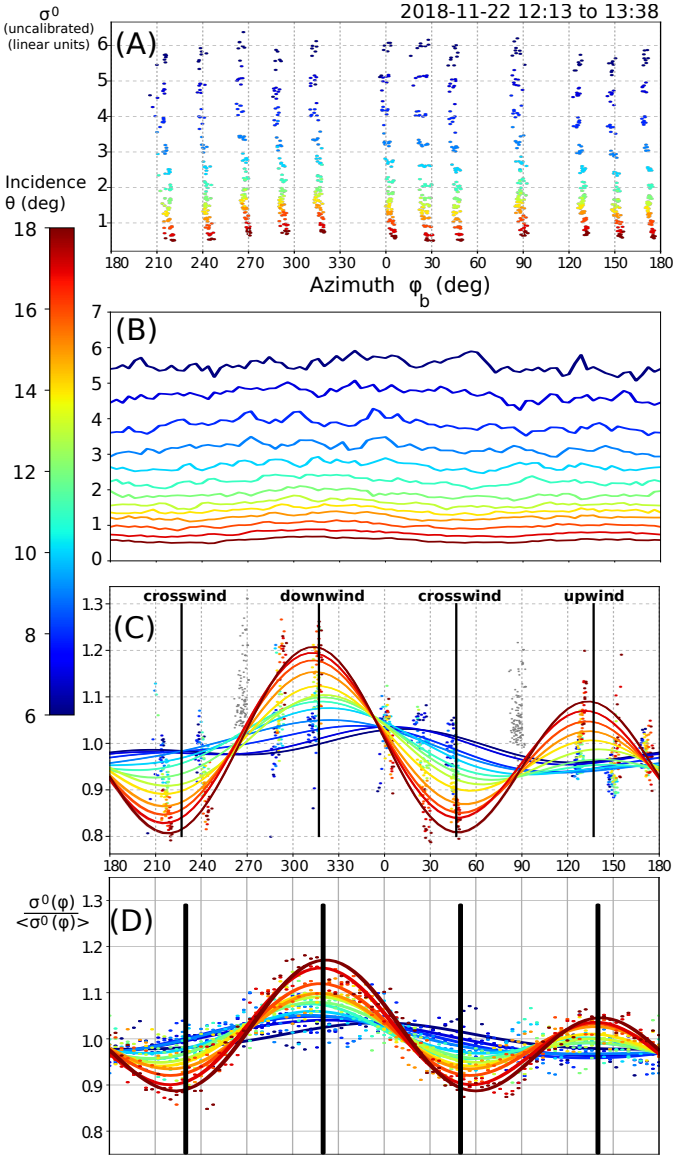

Figure 10. Azimuthal variation of σ^0 for incidences 6 to 18° on November 22. (A) and (B) are for the fixed and rotating antenna flights, respectively. (C) and (D) show σ^0 normalized by its average over all azimuths, with fixed and rotating antenna

The variation of σ^0 in Ku-band is shown for 22 November in Fig. 10, with one dot for each 30-s long record. These measurements show the expected azimuthal modulation of 0.8 to 0.9 dB with a downwind-crosswind contrast that increases from low to high incidence angle. This contrast is larger for the higher winds of 22 November. The Upwind-downwind asymmetry is expected from the behavior of the surface slope probability density function (Chapron et al., 2002; Walsh et al., 2008; Munk, 2008). The exception are the σ^0 values for the flight tracks with a fixed antenna around the azimuths 90 and 270 (Fig. 10.A),

https://doi.org/10.5194/os-2019-77
Preprint. Discussion started: 27 August 2019

Ocean Science
Discussions
Open Access
EGU

which have anomalous normalized values between 1 and 1.3 instead of expected values much closer to 1. We have no explanation yet for this anomaly. No such anomaly was found with the subsequent flight tracks of the same day in which the antenna was rotated (Fig. 10.B).

Discarding these azimuths (shaded in grey in figure 10.C), we fitted a functional variation of the form $a_0 + a_1 \cos(\varphi - \varphi_{\sigma,1}) + a_2 \cos[2(\varphi - \varphi_{\sigma,2})]$. As explained in section 2.1, this azimuthal variation is critical for the interpretation of the mean Doppler due to the spurious azimuth gradient Doppler velocity. As expected, the fitted directions $\varphi_{\sigma,1}$ and $\varphi_{\sigma,2}$ are very close to the wind direction, except for the lowest incidence angles for which the contrast is less than 0.05 dB.

On November 24, the σ^0 (Fig. 11) was much more uniform with azimuths, due to the much lower wind speed.

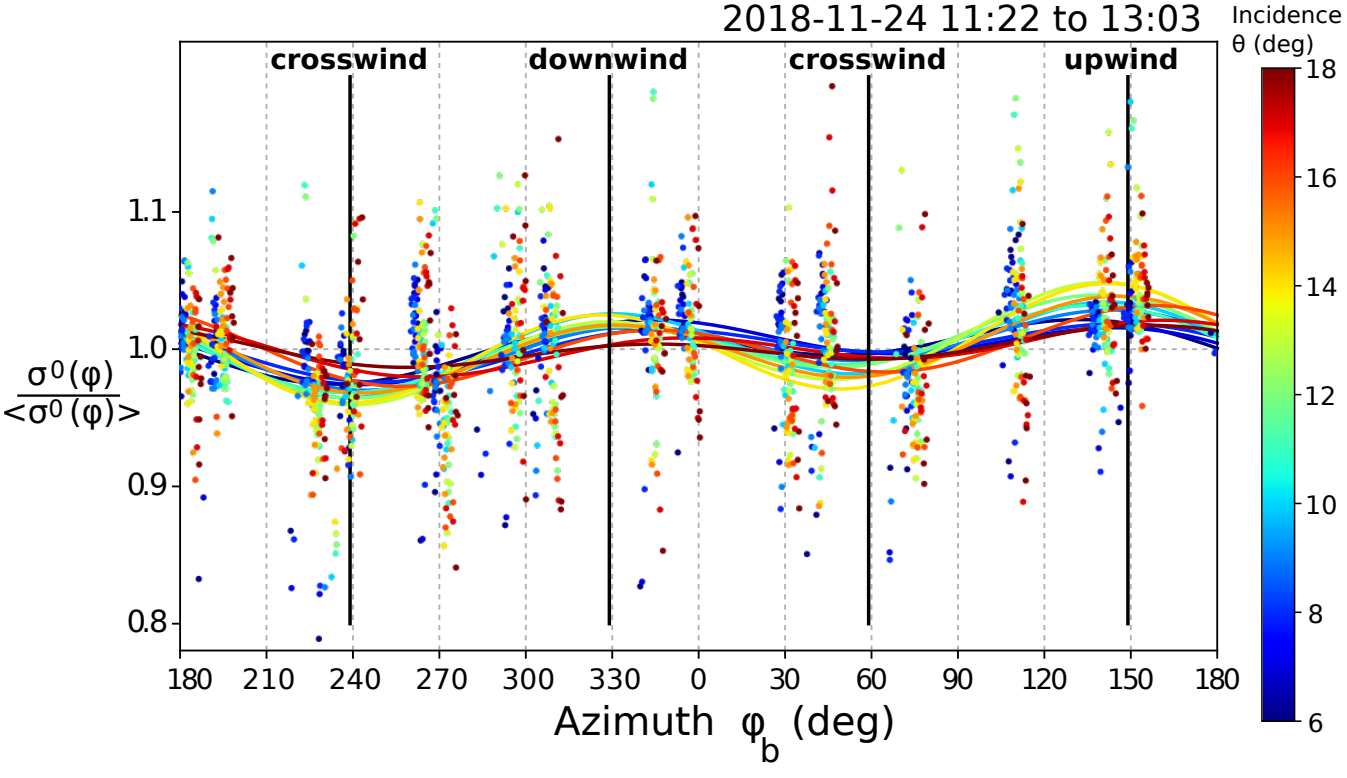

Figure 11. Same as Figure 10.C but on 24 November.

4.3 Mean Doppler from KaRADOC

We now discuss quantitatively the measured Doppler signal, in order to assess the agreement of our theory of the wave-induced Doppler U_{WD} with the measurements.

Starting with KaRADOC, easier to interpret than KuROS thanks to its narrower beam, we first examine the consistency of all the data acquired at an incidence of 12°. Figure 12 contains all the mean Doppler measurements represented with an offset, with blue lines, from the plane ground track (black lines). If the Doppler were the radial projection of a fixed vector, then all the

https://doi.org/10.5194/os-2019-77
Preprint. Discussion started: 27 August 2019

Ocean Science
Discussions
Open Access
EGU

blue lines would be straight, crossing at a single point. For November 22, 16 flight tracks are available, collected from 12:13 to 12:59 (TU), and 17 for November 24, collected from to 11:27 to 13:13 (TU).

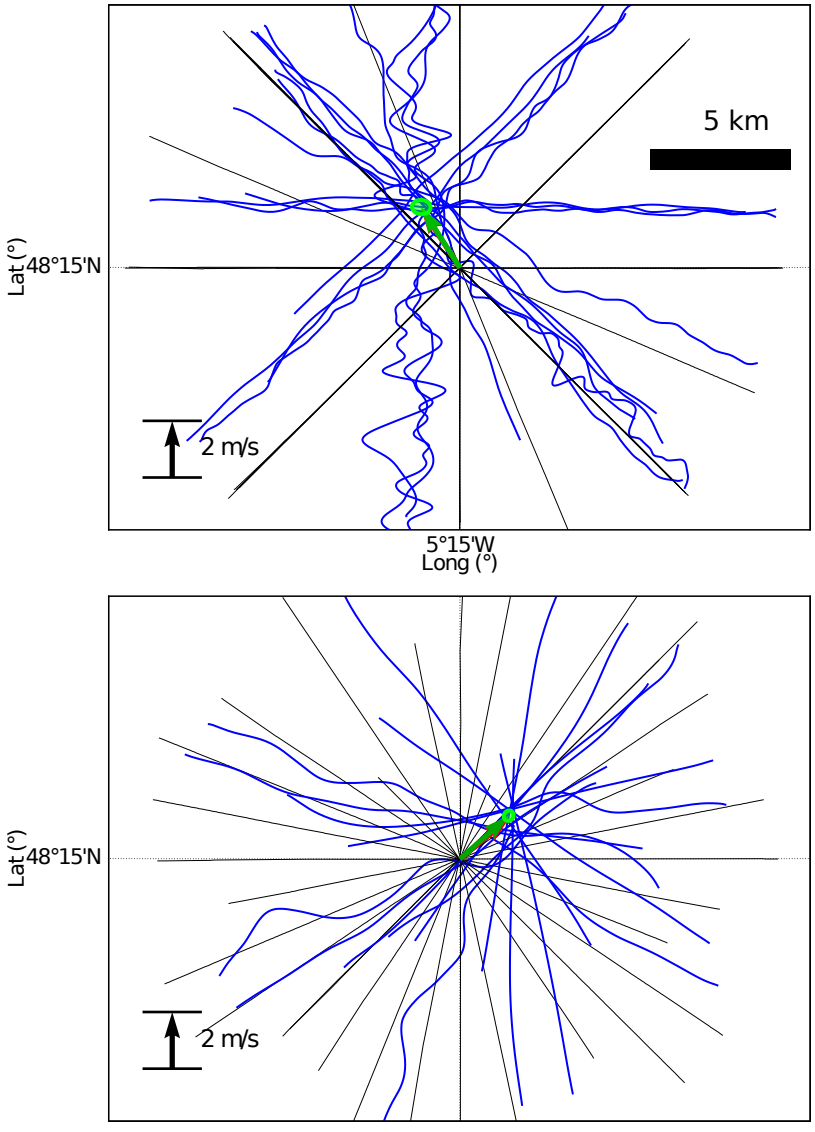

Figure 12. Plots of the Ka-band Doppler signal on (top) 2018/11/22 and (bottom) 2018/11/24. The flight tracks are marked as thin black lines. For each flight track, a thick blue line shifted to the right of the flight path by an amount proportional to the instantaneous Doppler represents the projection of the $\mathbf{U}_{\mathrm{GD}}$ vector along the instrument line-of-sight. At the beginning of each track data were discarded until the plane stabilized. The green arrow represents the maximum-likelihood estimate of the $\mathbf{U}_{\mathrm{GD}}$ vector using the whole data set. The red arrow shows the result of the least-squares sinusoidal fits shown in figures 13A and 13B. The 1-standard deviation error ellipse on the maximum-likelihood estimate is represented in green.

https://doi.org/10.5194/os-2019-77
Preprint. Discussion started: 27 August 2019

Overall, the assumption of a constant vector is good to within 0.3 m/s. It is particularly striking that the three horizontal lines in 12.A are almost perfectly aligned, corresponding to 2 flight tracks looking into azimuth 0° and one flight into azimuth 180°. On November 22, the largest uncertainty is for the 315° and 135° azimuths for which a total of 4 tracks are available with very different values that are consistent along each track.

Now using the average value for each track, we compare the measured Doppler velocity to the forward model given by eq. (1) with U_{WD} estimated from in situ wave buoy data using the model of Nouguier et al. (2018). The method combines the buoy spectrum up to 0.4 Hz and adds a high frequency tail based on Elfouhaily (1997), as detailed in LOPS (2019). The current contribution U_{CD}, is taken to be the drift velocity of the nearest CARTHE drifter, which is uniform to within 3 cm/s in the Offshore box (The following link https://odl.bzh/eVRHv1TE provides an interactive animation of all deployments and trajectories).

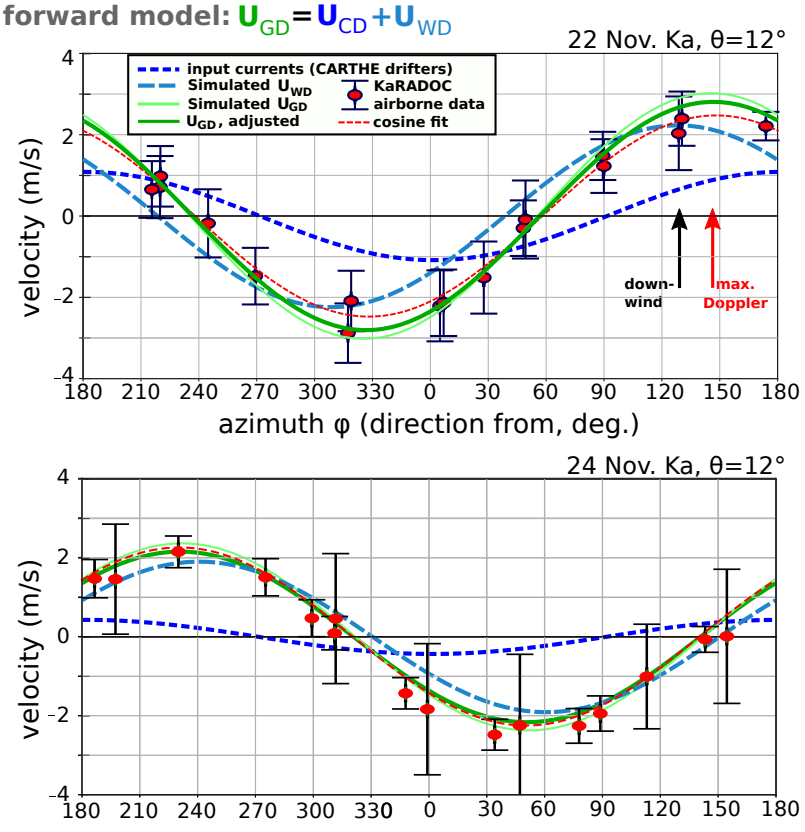

Figure 13. KaRADOC Doppler velocity (red circles) for the star-pattern flight of (Top) 22 and (Bottom) 24 November, and cosine function fit to the data (red line) that would be consistent with the radial projection of a vector. These are compared to modeled geophysical Doppler U_{GD} and an adjusted U'_{GD} in green, where the adjustment is a constant factor 10% reduction of U_{WD}. The modeled U_{GD} is the sum of the CARTHE drifter velocity U_{CD} in short dashed dark blue blue and the wave Doppler estimated from measured spectra, U_{WD}, in longer and lighter blue dashes

https://doi.org/10.5194/os-2019-77
Preprint. Discussion started: 27 August 2019

Figure 13 shows the measured mean Doppler and standard deviation for each track. On November 22, the current vector accounts for less than half of the observed magnitude of U_{GD} and it is interesting that the maximum Doppler velocity is from azimuth 144, in between the wind direction (130°) and the current direction (182°). The direction of the modeled and measured U_{GD} are within 5° of each other.

Compared to the relatively high wind condition on November 22, it is interesting to discuss the results for November 24 (Fig. 13, with a wind speed of 6 m/s instead of 11 m/s. The amplitude of the Doppler velocity are not much reduced, in spite of a more than halved current and Stokes drift. This is consistent with the expected near-constant value C_0 of the wave Doppler magnitude, and this is the main result of the present paper.

Looking in details, we find that the model gives larger values of U_{GD} than what is observed for both days. An ad hoc reduction of U_{WD} by 10% gives the best agreement between model and data. With such a reduction, the surface current vector is accurately inverted from the data, when $\mathbf{U}_{\mathrm{WD}}$ is subtracted off the fitted $\mathbf{U}_{\mathrm{GD}}$, as shown in figure 14.

The reason for the 10% model overestimation is not clear, and it may be due to a particular processing of the airborne data or assumptions in the model. This second hypothesis was tested by varying the method for estimating U_{WD}. Table 3 gives a subset of model tests with varying the exact input spectrum.

The largest differences, of the order of 10%, were found when changing the transition frequency from 0.35 to 0.5 Hz with a general increase of the simulated U_{WD} values. This can be interpreted as the effect of the directional distribution in the Elfouhaily (1997) spectrum that is probably slightly too narrow for intermediate wavelengths 2-10 m. This effect was discussed for very specific cases by Peureux et al. (2018) and it is not yet clear if it is specific to the very young wind seas they observed, although it could explain some properties of L-band backscatter (Yueh et al., 2013). Other effects, in particular the non-linearity of the waves (e.g. Nouguier et al., 2009, 2015) may also contribute a few percent to the deviation of mean Doppler.

While testing different model settings for U_{WD}, we also estimated the importance of the swell. Although the swell has a limited contribution to the mean square slope, in the present case it contains 6% of the zonal Stokes drift component V_s. When projected on the Doppler velocity direction, this explains the increase by 4% of U_{WD} when the swell is removed in table 3 because the swell contribution is in the direction opposite to the wind sea and thus reduces U_s and U_{WD} (see also Yurovsky et al., 2019). This is more easily understood by looking at the contribution of the different spectral components to U_s. In practice, $U_s(\varphi)$ is the projection of the horizontal vector (U_s, V_s) in direction φ and can be obtained from the heave spectrum $E(k)$ of the sea surface and the first directional moments $a_1(k)$ and $b_1(k)$, or the associated mean direction $\varphi_1(k)$, which is the direction of the vector $(a_1(k), b_1(k))$ and spread $\sigma_1(k)$ (Kuik et al., 1988), that can be measured from drifting wave buoys,

$$\sigma_1(k) = \sqrt{2(1 - \sqrt{a_1^2(k) + b_1^2(k)})}. \tag{20}$$

Using the dispersion relation for linear surface gravity waves in deep water, $\sigma^2 = gk$ with g the acceleration of gravity, the Stokes drift contribution at each wavenumber is given by the following spectrum (Kenyon, 1969),

$$(F_x, F_y) = k\sqrt{k/g}(1 - 0.5\sigma_1^2)(\cos\varphi_1, \sin\varphi_1)E(k), \tag{21}$$

https://doi.org/10.5194/os-2019-77
Preprint. Discussion started: 27 August 2019

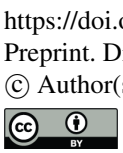

Ocean Science
Discussions
Open Access
EGU

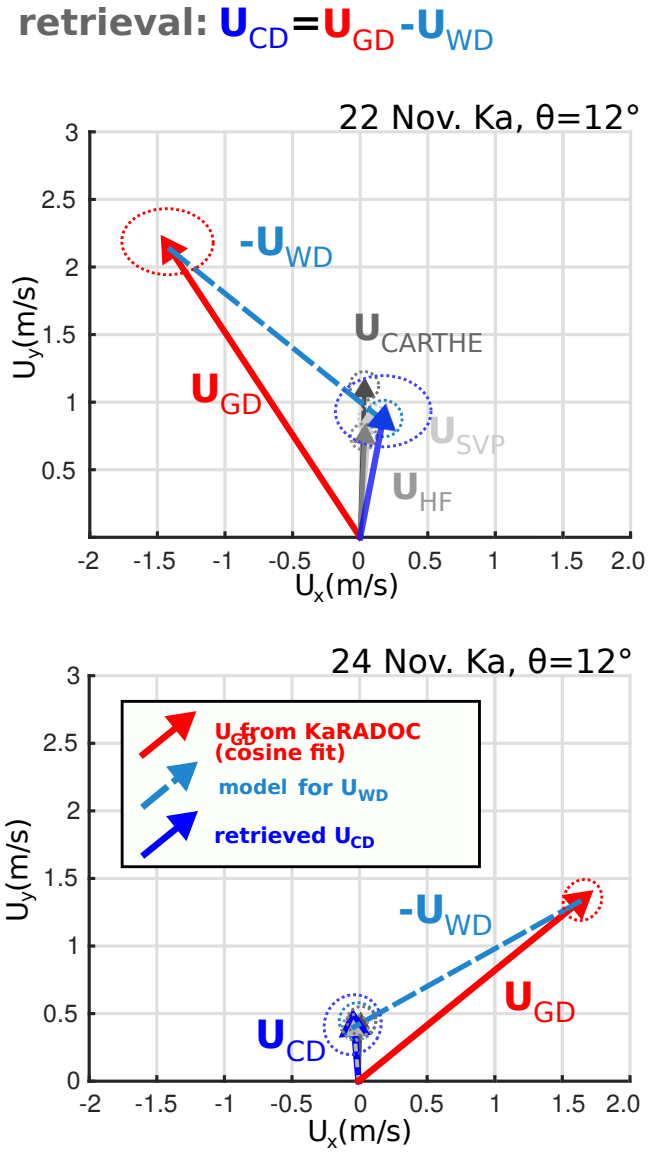

Figure 14. Retrieval of surface current vector U_{CD} in blue obtained by reducing U_{WD} by 10%, compared to in situ measurements by HF-radar, CARTHE and SVP drifter (three shades of grey).

which integrates to

$$(U_s, V_s) = \int_0^\infty (F_x, F_y)\mathrm{d}k. \tag{22}$$

https://doi.org/10.5194/os-2019-77
Preprint. Discussion started: 27 August 2019

Ocean Science
Discussions
Open Access
EGU

Table 3. Modeled wave Doppler amplitude M_{WD} and direction φ_{WD} using the same input spectra but varying the transition frequency f_t between the buoy spectrum and a Elfouhaily (1997) spectrum for the high frequencies, and the wave age Ω for this high frequency spectrum. Removing the swell from the input spectrum was also tested. Default values use $f_t = 0.35$ Hz and $\Omega = 0.83$. All values are estimated for an incidence angle $\theta = 12°$

22/11, 12:00 UTC			
wave spectrum	band	M_{WD} (m/s)	φ_{WD}
default	Ka	2.24	128.8
$\Omega = 1.3$	Ka	2.24	128.8
$\Omega = 2.5$	Ka	2.23	128.4
$f_t = 0.5$ Hz	Ka	2.43	127.5
$f_t = 0.5$ Hz,no swell	Ka	2.54	127.5
default	Ku	2.83	128.7
$\Omega = 1.3$	Ku	2.83	128.5
$\Omega = 2.5$	Ku	2.80	128.1
$f_t = 0.5$ Hz	Ku	2.97	129.2
$f_t = 0.5$ Hz, no swell	Ku	3.11	129.2
24/11, 12:00 UTC			
default	Ka	2.30	221.5
$\Omega = 1.9$	Ka	2.26	209.9
$\Omega = 2.5$	Ka	2.21	208.8
$f_t = 0.5$ Hz	Ka	2.26	207.6
default	Ku	2.56	211.4
$\Omega = 1.9$	Ku	2.51	209.5
$\Omega = 2.5$	Ku	2.45	208.4
$f_t = 0.5$ Hz	Ku	2.51	207.6

Figure 15 shows example of these spectra in the case of November 22, with a 2 m swell from the west, giving positive contributions to F_x for frequencies under 0.1 Hz (wavelengths larger than 150 m), and a wind-sea from the south-east, giving positive contributions to F_y and negative contributions to F_x.

Although the wind-sea energy is much less than that of the swell, its contribution, weighted by $k^{1.5} \propto f^3$ is much larger.

4.4 Mean Doppler from KuROS

Now looking at Ku-band data from KUROS, it is necessary to compute the NRCS azimuth gradient Doppler spurious velocity U_{AGD} due to the azimuthal variation of σ^0 across the KuROS wide antenna beam, as given by eq. (A35). In practice we use

https://doi.org/10.5194/os-2019-77
Preprint. Discussion started: 27 August 2019

Ocean Science
Discussions
Open Access
EGU

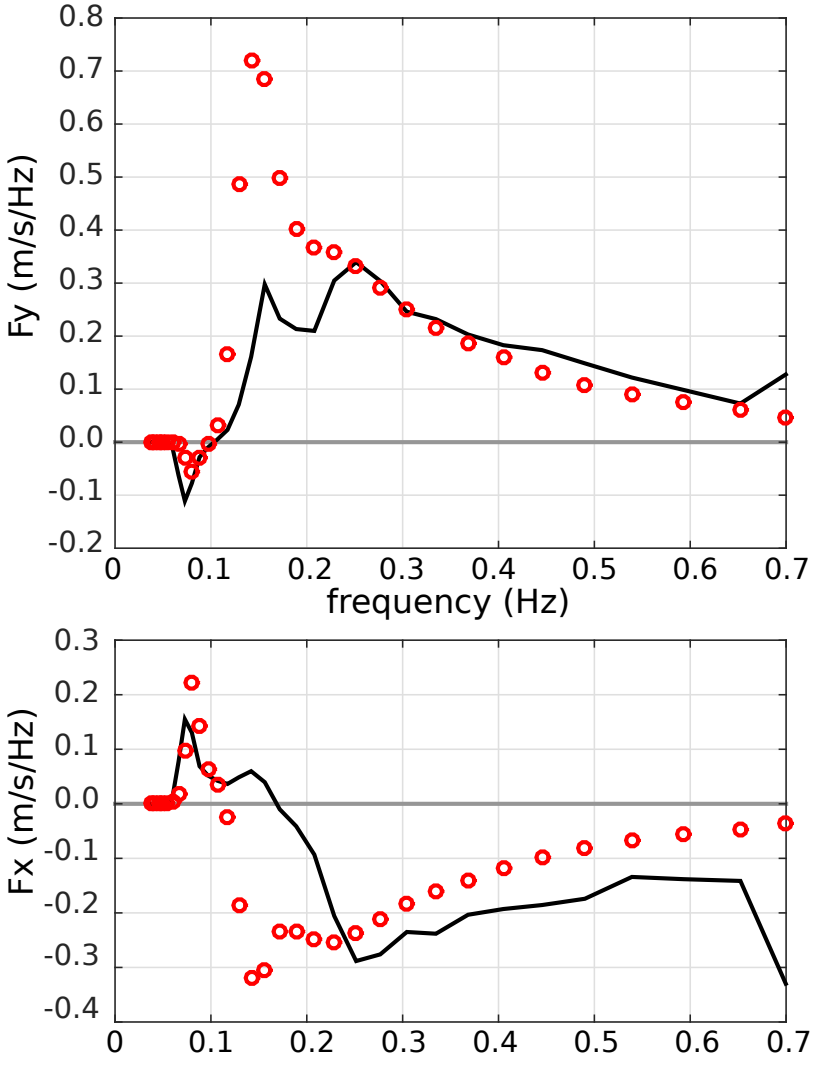

Figure 15. Spectra F_y and F_x of south-north and west-east Stokes drift components estimated from Trèfle buoy (solid line), on November 22, from 12:00 to 14:00 UTC, and modeled using WAVEWATCH III (red symbols).

a bi-harmonic form of σ^0 fitted to the measurements (Fig. 10) to compute U_{AGD}. As shown in Fig. 16.A,B, removing U_{AGD} reduces the maximum average velocities (from 4 to 3 m/s) that correspond to the saturated red patches in Fig. 9.D.

Still the measured Doppler velocities do not fit very well the forward model, in particular for the azimuths 210 to 300 degrees. The fit is still poor but relatively better at higher incidence angles, with 18° shown in Fig. 16.C. Given the lower importance of antenna lobe effects for higher incidences, it is quite possible that the mean Doppler deviations from the model are partly due to errors in the antenna pattern.

https://doi.org/10.5194/os-2019-77
Preprint. Discussion started: 27 August 2019

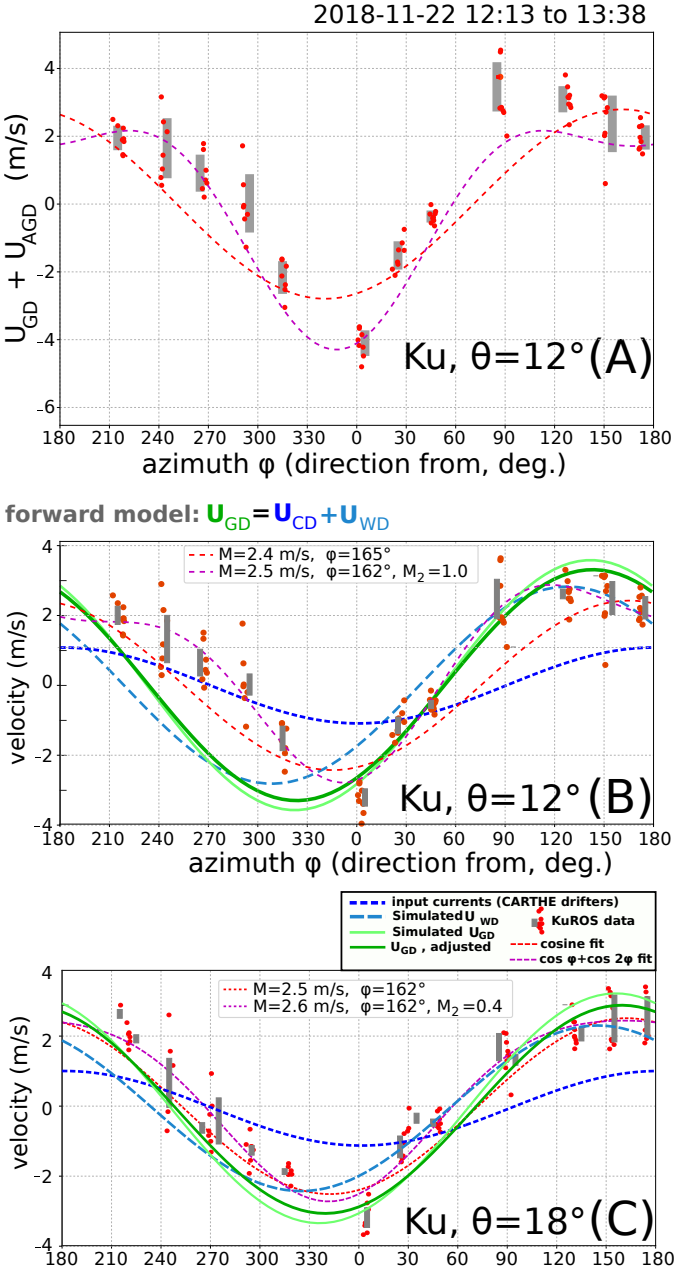

Figure 16. 30-s average Doppler velocity (red dots, grey bars are ± 1 standard deviation for a track) for the star-pattern flight of 22 November, (A) before correction of U_{AGD} for $\theta = 12^{\circ}$, (B) after correction of U_{AGD} for $\theta = 12^{\circ}$ and (C) after correction of U_{AGD} for $\theta = 18^{\circ}$. On each panel two fits are shown with a single cosine function and with a cosine and harmonic, as well as the expected signature of the current vector measured with CARTHE drifters (dark blue), the theoretical signature of the waves (light blue), the sum of the two (light green) and the sum with a 10% reduced U_{WD} (dark green).

https://doi.org/10.5194/os-2019-77
Preprint. Discussion started: 27 August 2019

Another issue is the general magnitude of the measured U_{GD} that is smaller with KuROS compared to KaRADOC, whereas theory would suggest the contrary. In particular, the wave Doppler, in a first approximation is ratio of the wave Stokes drift and the effective mean square slope $\mathrm{mss}_{\mathrm{shape}}$ as defined by Nouguier et al. (2016). With the known reduction of $\mathrm{mss}_{\mathrm{shape}}$ from Ka to Ku band, this should lead to a higher value of U_{WD} and thus U_{GD}. The KuROS data thus appear anomalous.

As a result, any attempt to retrieve surface current vectors from KuROS is not very successful for most incidence angles, as shown in Figure 17 for $\theta = 12°$.

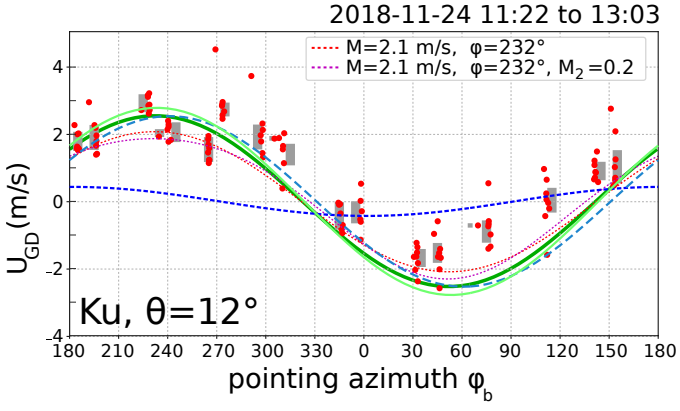

Figure 17. Same as Fig. 16.B, for November 24.

The amplitude of the Doppler velocity are not much reduced, in spite of a more than halved current and Stokes drift. This is consistent with the expected near-constant value C_0 of the wave Doppler magnitude. We also note that the upwind/downwind asymmetry of the Doppler is much reduced.

A simplified vector interpretation of the measured Doppler is shown in Fig. 18. It shows large differences, of the order of 50 to 100 cm/s between the KuROS estimates and the in situ measurements.

4.5 Observed Doppler modulations

In spite of issues related to the insufficient knowledge of the antenna pattern for a retrieval of the mean Doppler velocity, the KuROS measurement are very interesting for the analysis of the small scale velocity gradients. In particular, Caudal et al. (2014), with a different antenna (slightly narrower beam) had successfully used the cross-spectra of Doppler and NRCS to resolve the 180° ambiguity in the wave propagation direction. Also, an alternative to the theoretical model for U_{WD} used above, it may be possible to use the resolved part of the correlation between σ^0 and Doppler to estimate the unresolved part and the full U_{GD}.

In practice the Doppler modulations are also caused by the gradients of σ^0 and the speed of the aircraft, just like the mean spurious U_{AGD} velocity. These spurious modulations are enhanced by 70% when the antenna pattern is made 50% wider in azimuth, as illustrated in Figure 19. With typical variations of σ^0 up to 1 dB over scales of the order of 1 km (e.g. Fig. 9), the variation of σ^0 with azimuth φ is roughly proportional to $1/\sin\theta$ giving a U_{AGD} that does not vary much with θ, of the order of

https://doi.org/10.5194/os-2019-77
Preprint. Discussion started: 27 August 2019

Ocean Science
Discussions
Open Access
EGU

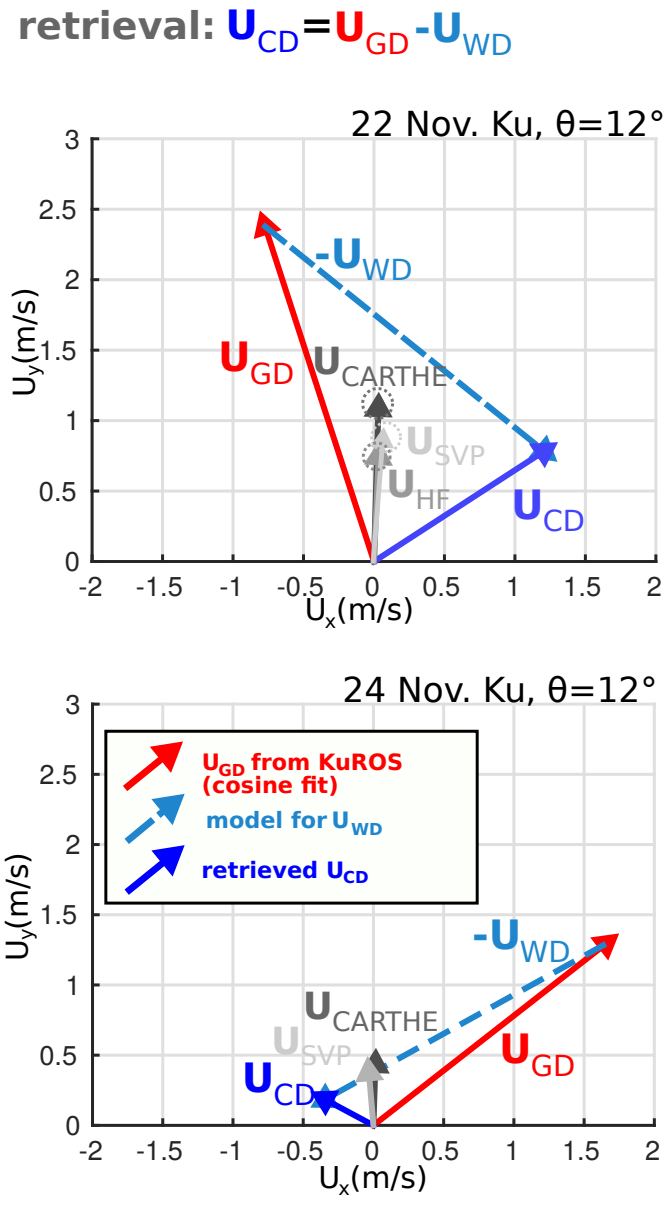

Figure 18. Comparison of KuROS-derived Doppler velocity, in situ (CARTHE, SVP drifters and HF radar) current measurements, and theoretical wave contribution U_{GD} including an *ad hoc* reduction of U_{WD} 10%.

1.5 m/s. This spurious velocity is larger than the 0.5 m/s significant orbital velocity of the swell. As a result the phase relation between Doppler and σ^0 can change sign as a function of azimuth, due to the combination of two imaging mechanisms with comparable magnitudes and possibly opposite signs.

https://doi.org/10.5194/os-2019-77
Preprint. Discussion started: 27 August 2019

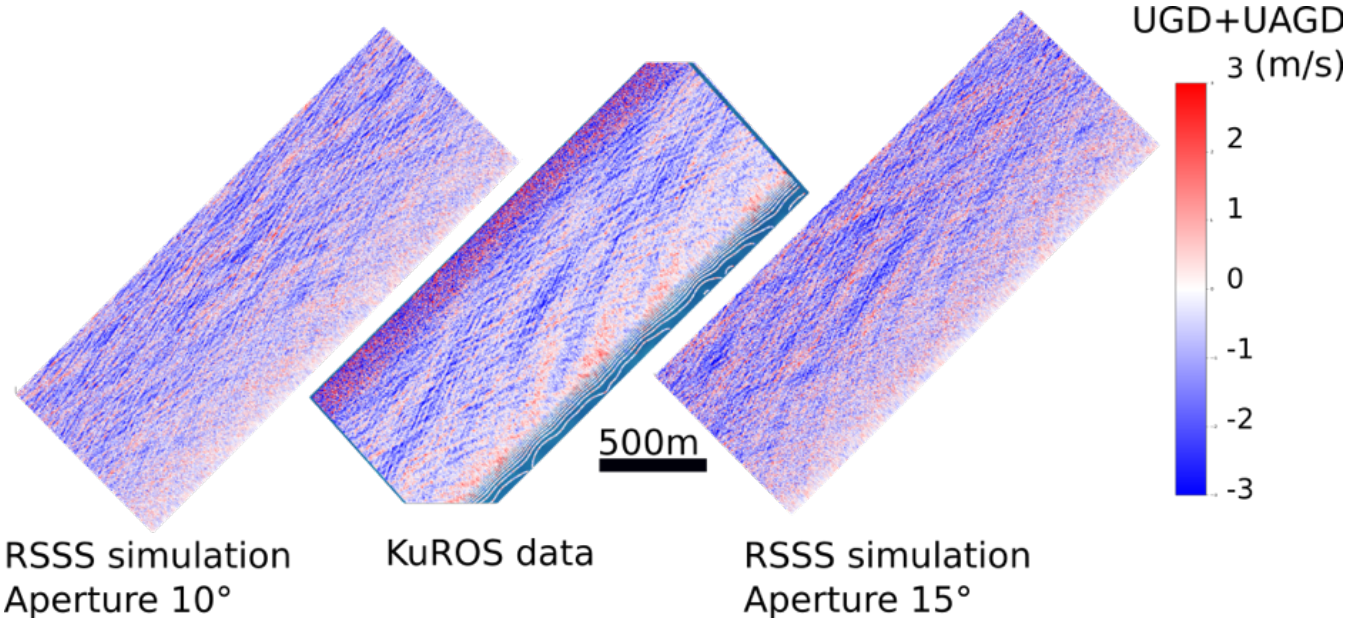

Figure 19. Qualitative validation of radar imaging mechanism in R3S simulations (Nouguier, 2019). Both the real data and simulation contain the geophysical modulation of velocities associated to surface velocities and slopes in the look direction (part of U_{GD}) and aircraft velocities and slopes in the flight direction (part of U_{AGD}). Note that the wave phases in the R3S simulation are random and cannot be expected to match those in the data or between the two simulations.

This effect will be weaker for shorter (wind sea) components as soon as the wavelength and crest length becomes much shorter than the KuROS footprint L_y, as given by eq. (6): for a given σ^0 contrast, the gradient increases linearly as the scale L is reduced, but the U_{AGD} for a given gradient is reduced exponentially in $-L_y/L$.

5 Implications for SKIM

The use of two Doppler radar, in Ka and Ku band, using the same pulse-pair technique but very different antenna patterns has provided important insight for the preparation of the SKIM mission.

In terms of radar measurement, the DRIF4SKIM campaign clearly demonstrated the robustness of the retrieval approach proposed for SKIM (Ardhuin et al., 2018; ESA, 2019), with the use of detailed wave spectrum measurements to estimate the wave Doppler contribution U_{WD}, associated to the wave intrinsic phase speed sensed through the surface slope spectrum. Accurate wave spectral measurements of the first directional moments, such as provided by a buoy, is sufficient to estimate U_{WD} and resolving wavelengths of 15 m (a frequency of 0.32 Hz) is generally sufficient to estimate the full spectral contribution, appending a parametric spectral shape of the unresolved shorter waves. In fact it is most important to resolve the peak of the windsea, and a resolved wavelength of 30 m is typically enough for wind speeds higher than 7 m/s.

https://doi.org/10.5194/os-2019-77
Preprint. Discussion started: 27 August 2019

Subtracting off U_{WD} from the measured geophysical Doppler provides an estimate of the total surface current velocity U_{CD}. This velocity is expected to be representative of the top meter of the ocean as given by the depth of measurement for each monochromatic wave train (Stewart and Joy, 1974), weighted by the slope spectrum. This velocity should contain most of the Stokes drift (Barrick and Weber, 1977; Broche et al., 1983; Ardhuin et al., 2009). As a result the velocity from any near-nadir Doppler Wave and Current Scatterometer, such as SKIM, is expected to give values between those of CARTHE drifters and a 12 MHz HF radar, consistent with the results shown in figure 18.

The campaign also stressed the necessity of a very good knowledge of the measurement geometry, including antenna pattern, and the spatial and azimuthal variation of the radar cross-section. In this respect, the main characteristics of the present campaign and planned SKIM satellite mission are recalled in table 4.

Table 4. Main differences between airborne KaRADOC and KuROS system as used in the present paper, and the SKIM system as presented by ESA (2019). The factor $\sigma_\varphi^2 \sin\theta V_p/2$ is the common factor that, multiplied by $\sin\varphi\partial(\log(\sigma^0))/\partial\varphi$ gives the spurious velocity U_{AGD}, given by eq. (A35)

	KuROS 12°	KaRADOC 12°	SKIM 12°	SKIM 6°
Altitude (km)	3	3	832	832
platform velocity V_p (m/s)	120	120	7000	7000
Beam width ($\alpha_{-3\mathrm{dB}}$) in degrees	15.0	1.85	0.65	0.58
half beam width on ground σ_φ	30.6	3.8	1.32	2.35
$\sigma_\varphi^2 \sin\theta V_p/2$ (m/s)	3.5	0.054	0.39	0.61

A true mispointing in azimuth δ_φ gives a spurious velocity $V_p\delta_\varphi \sin\varphi$, and aircraft velocities lead to much less strict requirements than satellite systems for which a pointing accuracy of a few microradians cannot be achieved by attitude measurements alone (gyroscopes and star-trackers) but uses a separation of the geophysical and non-geophysical patterns in the data (ESA, 2019). This data-driven approach is also used in airborne systems for correcting phase biases in the antenna pattern (Rodríguez et al., 2018, see also Appendix D).

The apparent mispointing due to σ^0 gradients in azimuth or space is proportional to the beam width squared, and leads to larger non-geophysical velocities for KuROS at 12° incidence, than for SKIM, even at 6°. That effect however is practically negligible for KaRADOC at 12°, as shown in figure 2.

Finally we recall that the incidence angle is estimated from the range measurement in the case of KuROS and from the highly directive antenna pattern for KaRADOC. Translated to SKIM, which uses range measurements like KuROS, it requires a knowledge of the local slope of the ocean as the nearest ocean target for the nadir beam is not exactly at nadir but slightly offset due to the geoid slope, up to 300 microradians (Sandwell and Smith, 2014) and more importantly the sea surface height difference between the nadir and the oblique beams.

Other radar system constraints or optimizations for satellite systems are discussed by Rodriguez (2018) and (ESA, 2019, chapter 5), with sampling issues further analyzed by Chelton et al. (2019).

https://doi.org/10.5194/os-2019-77
Preprint. Discussion started: 27 August 2019

6 Conclusions and perspectives

Although it was the first deployment of the KaRADOC instrument and only a limited dataset could be acquired due to the necessary adjustment process, the DRIF4SKIM campaign clearly demonstrated that surface geophysical velocities can be measured by a pulse-pair method with a Ka-band measuring at 12° incidence. The campaign data are consistent, with a 10% bias, with a Geophysical Model Function (GMF) that expresses the geophysical Doppler as the sum of the range component of the Total Surface Current Velocity, and a Wave Doppler that is a weakly varying function of the sea state, of the order of 2.5 m/s. This wave Doppler is analogous to the Bragg velocity contribution in HF radars but it integrates all wavenumbers and directions, weighted by the surface slope spectrum.

For 11 m/s winds, the difference in drift velocity between CARTHE and SVP drifters and HF radar, of the order of 20 cm/s, is not due to a large scale vertical shear, and may be associated to either a particular behaviour of CARTHE drifters in wave motions, or some shear in the top meter. This will be further investigated elsewhere using the 30 cm depth measurements of the Trèfle buoy (which capsized on November 21 in the present experiment).

In general, the robustness of the theoretical GMF and its possible empirical adaptation will require the acquisition of more data in a wider range of wind and wave conditions.

Finally, the test of near-nadir satellite measurements is limited by the very different viewing geometry due to the difference in altitude. Airborne measurement footprints are at most 500 m or so, and thus cannot reproduce the averaging properties of a much wider footprint from a satellite. Still, this medium-sized footprint is comparable to the unfocused SAR resolution that will be obtained with SKIM and provides some practical application with a similar azimuthal averaging that has a limited directional resolution for swell spectrum measurement. This limited azimuthal resolution is probably sufficient for estimating parameters such as the Stokes drift given by eq. (22) and does not require a full turn of the antenna to observe all waves, thereby making possible a higher spatial resolution of the Stokes drift vector.

Future airborne systems may ideally combine higher incidence angles such as used on DopplerScatt (Rodríguez et al., 2018) and OSCAR/Wavemill (Martin et al., 2018), with near-nadir angles that allow unambiguous wave measurements. In that case, the large azimutal footprint of KuROS is probably not necessary, and a narrower beam like KaRADOC can be used, greatly simplifying the analysis of antenna beam patterns.

Code and data availability. Data and numerical model results presented in this article are available via ftp at the following address: http://tinyurl.com/SKIMftp

https://doi.org/10.5194/os-2019-77
Preprint. Discussion started: 27 August 2019

Ocean Science
Discussions
Open Access
EGU

Appendix A: Pulse Pair theory

A1 Radar pulse-pair measurements

A radar instrument works by sending microwave pulses into the environment, and recording the echo. Usual scatterometers consider only the intensity of the return signal. Coherent instruments, such as SARs, measure both the amplitude of the return signal and its phase with respect to the transmitted carrier, as a function of range. Over the ocean, the phase of the return signal for a single pulse is random and uniformly distributed over the unit circle. The radar returns of successive pulses transmitted at short intervals are however correlated, and the time history of the phase can be used to measure the relative motion of the radar and the scatterers. SARs make use of this property to refine the along-track resolution of backscattering cross-section measurements. SKIM and the other proposed Doppler missions aim to use it to obtain direct surface current measurements.

As explained by Rodriguez (2018, Appendix A), the complex amplitude of the return signal of a pulse transmitted at time t_i can be expressed as

$$E_i(t_i,r') = n(t_i,r') + \frac{A(r')}{r'^2}\times \int dS\, G(t_i,\mathbf{x})\chi(r'-r(t_i,\mathbf{x}))\exp\left[-2ikr(t_i,\mathbf{x})\right] s(t_i,\mathbf{x}), \quad \text{(A1)}$$

where the integral is performed over the sea surface; $A(r')$ is a time-independent weakly-dependent function of range, unimportant for our purposes here (corresponding in particular to the effects of transmitted signal amplitude, receiver and processing gain and attenuation losses); $G(\mathbf{x})$ is the one-way antenna pattern; $\chi(r)$ is the range point-target response of the instrument; r' is the nominal pixel range in the time sampled signal; $k = 2\pi/\lambda$ is the radar wavenumber; $r(t_i,\mathbf{x})$ is the range from the radar to the observation point $\mathbf{x}$ at time t_i; $n(t_i,r')$ is the thermal noise contribution, and $s(t_i,\mathbf{x})$ is the complex reflection coefficient of the sea surface at instant t_i and location $\mathbf{x}$.

As mentioned by Rodríguez et al. (2018), the thermal noise contribution, though it plays a major role in setting the quality of the measurements, poses no great conceptual difficulty, and can be safely considered as δ-correlated in time, and characterized by a single quantity, its average power N. The reflection coefficient $s(t_i,\mathbf{x})$, on the other hand, emerges from the interaction of the electromagnetic waves with the ocean surface, and has a much richer physics. It is affected by electromagnetic phenomena, by the geometry and kinematics of the sea surface itself, and its statistics are further complicated by the so-called "speckle" phenomenon. As stated by Rodríguez et al. (2018) the correlation function of this coefficient as a function of time and space separation, averaging over speckle realizations, can be modelled as

$$\langle s(t,\mathbf{x})s^*(t',\mathbf{x}')\rangle_S = \delta(\mathbf{x}-\mathbf{x}')\sigma^0(t,\mathbf{x})\gamma_{TS}(|t-t'|), \quad \text{(A2)}$$

with $\sigma^0(t,\mathbf{x})$ the Normalized Radar backscattering Cross Section (NRCS) in the appropriate polarization, and $\gamma_{TS}(|\tau|)$ a function describing its time decorrelation at a fixed location, due to the life history of individual scattering patches.

Combining expressions (A1) and (A2) to compute the speckle-averaged product of the return signals for two consecutive radar pulses sent at t_1 and $t_2 = t_1 + \Delta t$, with Δt the pulse repetition interval (PRI), one obtains

$$PP_{\Delta t}(t_1,r') = \langle E_2(t_2 = t_1+\Delta t, r')E_1(t_1,r')^*\rangle_S$$

https://doi.org/10.5194/os-2019-77
Preprint. Discussion started: 27 August 2019

Ocean Science
Discussions
Open Access
EGU

as

$$PP_{\Delta t}(t_1, r') = \frac{A^2(r')}{r'^4} \times \gamma_{TS}(|\Delta t|) \times \int \chi^2(r' - r(t_1, \mathbf{x}))\, G^2(t_1, \mathbf{x})\, \sigma^0(t_1, \mathbf{x}) \times \exp\left[-2ik\left[r(t_1 + \Delta t, \mathbf{x}) - r(t_1, \mathbf{x})\right]\right] dS. \quad \text{(A3)}$$

The phase of eq. (A3) contains a weighted average of the time rate-of-change of the distance separating the radar from the scattering elements in its instantaneous footprint. This rate of change can be interpreted as a velocity and this method is the so-called "Pulse-Pair" technique of Zrnic (1977).

A2 Measurement geometry

Figures 1A and 1B summarize the acquisition geometry in the airborne and space-borne settings. The influence of the antenna radiation diagram $G^2(t_1, \mathbf{x})$ is represented as a grey shading of the sea surface, while the influence of the range point-response function $\chi^2(t_1, r' - r(t_1, \mathbf{x}))$ is represented as the grating in white. In eq. (A3), we have made the assumptions that $G(t_1, \mathbf{x}) = G(t_2, \mathbf{x})$, and $\chi(r' - r(t_1, \mathbf{x})) = \chi(r' - r(t_2, \mathbf{x}))$, neglecting the effect of the spatial translation of the beam illumination pattern and range-resolution weighting distribution on the sea surface.

This is a very good approximation for airborne pulse-pair radar observations, and a quite good one for spaceborne observations. For airborne instruments, the PRI is usually chosen such that the line-of-sight projection of the platform movement over a PRI is smaller than one-half wavelength to avoid phase ambiguity. For space-borne instruments, avoiding ambiguity is not practical, due to the much larger platform velocity, but the PRI is constrained by other considerations, and the platform displacement over a PRI is much smaller than the characteristic scales of the antenna radiation diagram as well as of the range point-response.

A2.1 Pulse-pair signal approximation

Returning to expression (A3), we see that over the time interval separating the two radar pulses, the radar has moved from its original position $\mathbf{x}_R(t_1)$ to $\mathbf{x}_R(t_1) + \mathbf{V}_P \Delta t$, and the scatterers originally located at $\mathbf{x}$ have moved to $\mathbf{x} + \mathbf{v_s} \Delta t$ (specifying the reference frame is not yet necessary since only relative separations are important at this stage). The radar-to-scatterers vector has thus changed by $[\mathbf{v}_s(\mathbf{x}) - \mathbf{V}_P]\,\Delta t$. The distance change can be approximated by

$$r(t_1 + \Delta t, \mathbf{x}) - r(t_1, \mathbf{x}) = \Delta t \frac{\mathbf{x} - \mathbf{x}_R(t_1)}{||\mathbf{x} - \mathbf{x}_R(t_1)||} \cdot (\mathbf{v}_s - \mathbf{V}_R), \quad \text{(A4)}$$

where neglected are of the order of $\Delta t^2 ||\mathbf{v}_s - \mathbf{v}_R||^2 / ||\mathbf{x} - \mathbf{x}_R(t_1)||^2$. Introducing

$$\mathbf{e}(\mathbf{x}) = \frac{\mathbf{x} - \mathbf{x}_R(t_1)}{|\mathbf{x} - \mathbf{x}_R(t_1)|} \quad \text{(A5)}$$

https://doi.org/10.5194/os-2019-77
Preprint. Discussion started: 27 August 2019

the unit vector pointing from the radar location at t_1 to the observation point (choosing either time instant is equivalent, as the difference is of the same order of magnitude as the neglected terms), the pulse-pair signal can be expressed as

$$PP_{\Delta t}(t_1,r') = \frac{A^2(r')}{r'^4} \times \gamma_{TS}(\Delta t) \times$$
$$\int G^2(t_1,\mathbf{x})\, \chi^2(r' - r(t_1,\mathbf{x}))\, \sigma^0(t_1,\mathbf{x}) \times$$
$$\exp\left[2ik\, \Delta t\, \mathbf{e}(\mathbf{x}) \cdot (\mathbf{V}_R - \mathbf{v}_s(\mathbf{x}))\right] dS. \quad \text{(A6)}$$

This equation is not very practical, as the relative motion of the scatterers with respect to the radar enters as the argument of exponential contributions to an integral. Obtaining an equivalent representation as the exponential of a sum of weighted integrals would be desirable. Introducing the effective illuminated surface

$$S(t_1,r') = \int G^2(t_1,\mathbf{x})\, \chi^2(r' - r(t_1,\mathbf{x}))dS, \quad \text{(A7)}$$

the normalized weighting function

$$W(t_1,r',\mathbf{x}) = \frac{G^2(t_1,\mathbf{x})\, \chi^2(r' - r(t_1,\mathbf{x}))}{S(t_1,r')}, \quad \text{(A8)}$$

the average and fluctuating parts of the NRCS

$$\overline{\sigma^0}(t_1,r') = \int W(t_1,r',\mathbf{x}) \sigma^0(t_1,\mathbf{x}) dS, \quad \text{(A9)}$$

$$\widetilde{\sigma^0}(t_1,r') = \frac{\sigma^0(t_1,\mathbf{x})}{\overline{\sigma^0}(t_1,r')}, \quad \text{(A10)}$$

and borrowing the algebraic technique of "cumulant expansion" from probability theory, it is possible to express $PP_{\Delta t}$ as

$$PP_{\Delta t}(t_1,r') = \frac{A^2(r')}{r'^4} \times \gamma_{TS}(\Delta t) \times \overline{\sigma^0}(t_1,r') \times S(t_1,r')$$
$$\times \exp\left[\sum_{n=1}^{\infty} \frac{(\mathrm{i}2k\Delta t)^n}{n!} \kappa_n\right], \quad \text{(A11)}$$

with κ_n the successive "cumulants" of $\mathbf{e}(\mathbf{x}) \cdot (\mathbf{V}_R - \mathbf{v}_s(\mathbf{x}))$ with respect to the "density distribution" $\widetilde{\sigma^0}(t_1,\mathbf{x}) W(t_1,r',\mathbf{x})$. As all the κ_n are real, we see that odd-n terms contribute to the argument of the pulse-pair signal, while even-n terms contribute to its magnitude. Keeping only the first two terms in the sum, one obtains:

$$PP_{\Delta t}(t_1,r') = \frac{A^2(r')}{r'^4} \times \gamma_{TS}(\Delta t) \times \overline{\sigma^0}(t_1,r') \times S(t_1,r')$$
$$\times \exp\left[\mathrm{i}2k\Delta t\kappa_1\right] \times \exp\left[-2(k\Delta t)^2\kappa_2\right]. \quad \text{(A12)}$$

As expected, the expression of κ_1,

$$\kappa_1(t_1,r') = \quad \text{(A13)}$$
$$\int W(t_1,r',\mathbf{x})\, \widetilde{\sigma^0}(t_1,\mathbf{x})\, \mathbf{e}(\mathbf{x}) \cdot (\mathbf{V}_R - \mathbf{v}_s(\mathbf{x}))\, dS \quad \text{(A14)}$$

https://doi.org/10.5194/os-2019-77
Preprint. Discussion started: 27 August 2019

shows that to first order the argument of the pulse-pair signal gives access to the integral over the footprint of the relative velocity of the scatterers with respect to the radar. The expression of κ_2,

$$\kappa_2 = \int W(t_1, r', \mathbf{x})\, \widetilde{\sigma^0}(t_1, \mathbf{x})\, \left[\mathbf{e}(\mathbf{x}) \cdot (\mathbf{V}_R - \mathbf{v}_s(\mathbf{x})) - \kappa_1\right]^2 dS, \tag{A15}$$

is a description of the impact of the variability of $\mathbf{e}(\mathbf{x})$, $\widetilde{\sigma^0}$ and $\mathbf{v}_s$ inside the footprint on the pulse-pair signal magnitude.

A2.2 Pulse-pair signal phase approximation

Selecting a frame of reference, we define

$$V_{\mathrm{GD}} = -\int W(t_1, r', \mathbf{x})\, \widetilde{\sigma^0}(t_1, \mathbf{x})\, \mathbf{e}(\mathbf{x}) \cdot \mathbf{v}_s(\mathbf{x})\, dS \tag{A16}$$

the (geophysically relevant) weighted projection of the scatterers velocity in that frame on the radar line-of-sight and

$$V_{\mathrm{NG}}(t_1, r') = \mathbf{V}_R \cdot \int W(t_1, r', \mathbf{x})\, \widetilde{\sigma^0}(t_1, \mathbf{x})\, \mathbf{e}(\mathbf{x})\, dS \tag{A17}$$

the (geophysically irrelevant) projection of the radar velocity. (Our conventions are such that V_{GD} is positive when the scatterers move towards the radar, and that V_{NG} is positive when the radar moves towards the footprint, in keeping with everyday intuition).

With these conventions, one sees that:

$$V_{\mathrm{GD}}(t_1, r') = \kappa_1(t_1, r') - V_{\mathrm{NG}}(t_1, r'). \tag{A18}$$

Using equation (A12), one can obtain κ_1 approximately as $1/(2k\Delta t)$ times the argument of the complex pulse-pair signal. To do so, one must however consider a bit carefully the ambiguity that is inherent in phase measurements. For airborne instruments it is usually feasible to select a small enough PRI to avoid ambiguity altogether. For satellite instruments, one approach is to select a solid Earth fixed reference frame, in which $\mathbf{v}_s$ is small, and to work on the phase-migrated pulse pair signal

$$\widetilde{PP}_{\Delta t}(t_1, r') = \exp\left[-\mathrm{i}2k\Delta t V_{\mathrm{NG}}\right] \times PP_{\Delta t}(t_1, r').$$

It is easy to see that V_{GD} can be retrieved as

$$V_{\mathrm{GD}}(t_1, r') = \frac{1}{2k\Delta t} \arg\left(\widetilde{PP}_{\Delta t}(t_1, r')\right).$$

At this stage, even a coarse approximation of V_{NG} can be used, as long as it is sufficient to resolve the phase ambiguity. This is important in particular for the onboard processors of satellite instruments, which have to rely on limited quality position/velocity/pointing information and typically can not use the $\widetilde{\sigma^0}$ distribution information ground segment processors can retrieve from the signal. Care must however be taken to take account of the correction applied by the onboard processor in later processing stages.

https://doi.org/10.5194/os-2019-77
Preprint. Discussion started: 27 August 2019

Ocean Science
Discussions
Open Access
EGU

A3 Non-geophysical Doppler V_{NG}

A3.1 Overview

This section will describe the different contributions to Non-geophysical Doppler (V_{NG}). At first order the signature is dominated by the platform velocity and its pointing knowledge. A second point is the determination of the range knowledge which is directly linked to the timing and altitude accuracy. This point is critical for pulse-limited instruments, as KuROS and SKaR, for which the pointing is determined for each range bin as function of the altitude. Last, asymmetric variation in NRCS within the antenna azimuth for a given range bin generate a bias in Doppler. All these three elements need to be accurately corrected in order to have an accurate geophysical Doppler measurement.

A3.2 Pointing knowledge

At this point of the discussion, we will leave the general setting and will start orienting our convention choices towards the description of the airborne case of the Drift4SKIM campaign. Problems specific to the space-borne case, such as the need to work in global-scope reference frames or to account for Earth rotation and sphericity, or structural details such as the parabolic reflector featured by the SKaR instrument, do not change the deep nature of the issues, but do introduce a heavy notational burden which tends to obscure the discussion.

From now on, we will work in the simplified setting of the flat-Earth approximation, in which the elevation and incidence angles γ and θ are equal. We will use a platform-fixed reference frame, the origin of which is located at the antenna phase center of the instrument, with x-vector pointing to the geometric front of the platform, y-vector pointing to starboard, and z-vector pointing to the floor, and a local geographic North/East/Down reference frame, the origin of which is fixed to the solid Earth and located at a suitable point of the campaign area.

The orientation of the platform-fixed reference frame with respect to the local geographic frame is provided by the platform IMU as (Roll, Pitch, Heading) Euler angles, from which one can construct the Direction Cosine Matrix:

$$\mathbf{DCM} = \begin{bmatrix} c_p.c_h & s_r.s_p.c_h - c_r.s_h & c_r.s_p.c_h + s_r.s_h \\ c_p.s_h & s_r.s_p.s_h + c_r.c_h & c_r.s_p.s_h - s_r.c_h \\ -s_p & s_r.c_p & c_r.c_p \end{bmatrix} \tag{A19}$$

allowing one to express the components of a vector in the (N, E, D) frame from its (x, y, z) components in the platform-fixed frame. The two reference frames are consistent in the sense that the frame vectors coincide when the platform is in level flight towards the North. In the above expression we have used the transparent notation $c_p \rightarrow \cos(\mathrm{pitch}), s_r \rightarrow \sin(\mathrm{roll}), c_h \rightarrow \cos(\mathrm{heading})$, etc... Other quantities worth introducing are the course c and glide angle g such that the plane velocity vector in the NED frame is

$$\mathbf{V}_R = V_R \left[\cos(g)\cos(c)\mathbf{N} + \cos(g)\sin(c)\mathbf{E} + sin(g)\mathbf{D}\right]. \tag{A20}$$

https://doi.org/10.5194/os-2019-77
Preprint. Discussion started: 27 August 2019

In the NED frame, the pointing vector $\mathbf{e}$ can be expressed as

$$\mathbf{e} = \sin(\theta)\,[\cos(\varphi)\mathbf{N} + \sin(\varphi)\mathbf{E}] + \cos(\theta)\mathbf{D}. \tag{A21}$$

Its components in the platform-fixed frame can be determined using the fact that $\mathbf{DCM}^{-1} = \mathbf{DCM}^{T}$. The corresponding antenna azimuth and elevation angles φ and γ, in terms of which the radiation diagram is specified, can then be expressed using the platform-fixed to antenna-fixed reference frame transformation matrix.

With these notations, and using eq. (A17), one can express V_{NG} as

$$V_{NG}(t_1, r') = V_R \int W(t_1, r', \mathbf{x})\, \widetilde{\sigma^0}(t_1, \mathbf{x}) \times [\cos(g)\sin(\theta)\cos(\varphi - c) + \sin(g)\cos(\theta)]\; dS. \tag{A22}$$

Level flight corresponds to $g \simeq 0$. We thus concentrate on the impact of errors in the first term of the RHS of this equation. Quite clearly, the impact of errors in $\sin(\theta)$ is largest when the instrument views the area where $\cos(\varphi - c)$ is large, *i.e* in the up/down-track directions, while the impact of errors in the azimuthal direction is largest when the instrument looks cross-track (i.e. where the derivative of $\cos(\varphi - c)$ is close to 1).

Leaving aside for the moment the effects of uncertainties on $W(t_1, r', \mathbf{x})$ and $\widetilde{\sigma^0}(t_1, \mathbf{x})$, one sees that at 12° incidence, and for a platform velocity of 7000 m/s (space-borne instrument), the SKIM 1 cm/s error budget on horizontal velocity measurements translates to pointing accuracies of 0.3 and 1.4 microradians in incidence and azimuth, respectively (these figures are obtained by allowing each of the pointing errors to consume the full error allocation. As the two terms reach their maximal amplitudes in different parts of the swath, this is not unreasonable). In the airborne case at 120 m/s platform velocity and 3000 m altitude, the corresponding numbers are 18 and 85 microradians for incidence and azimuth pointing accuracy for KuROS, respectively. In the cross-track viewing geometry of KaRADOC, only the comparatively mild (but still quite demanding) 85 microradians azimuth pointing accuracy requirement applies.

Figure (A1A) shows the measurement geometry, seen from above. One can see that uncertainties on the viewing azimuth and incidence have different origins:

– the uncertainty in azimuth can be due to an imperfect knowledge of the weighting corresponding to the $W(t_1, r', \mathbf{x})\, \widetilde{\sigma^0}(t_1, \mathbf{x})$ term in eq. (A22). This can of course come from imperfect platform attitude or antenna orientation information, but also from an imperfect characterization of the antenna radiation diagram or of the distribution of σ^0 on the sea surface.

– the uncertainty in incidence is due to an imperfect knowledge of the radial position of the range resolution bins (yellow striping of the footprint if fig. A1A). This can be due to an imperfect timing accuracy, or to an imperfect knowledge of the vertical separation between instrument and sea surface.

A3.3 Timing and altitude accuracy

For this brief discussion of the effects of timing and altitude accuracy on incidence angle estimation, we consider a single range bin whose "true" range from the radar is r, whose altitude with respect to the radar is H, and where the incidence angle is θ. In

https://doi.org/10.5194/os-2019-77
Preprint. Discussion started: 27 August 2019

Ocean Science
Discussions
Open Access
EGU

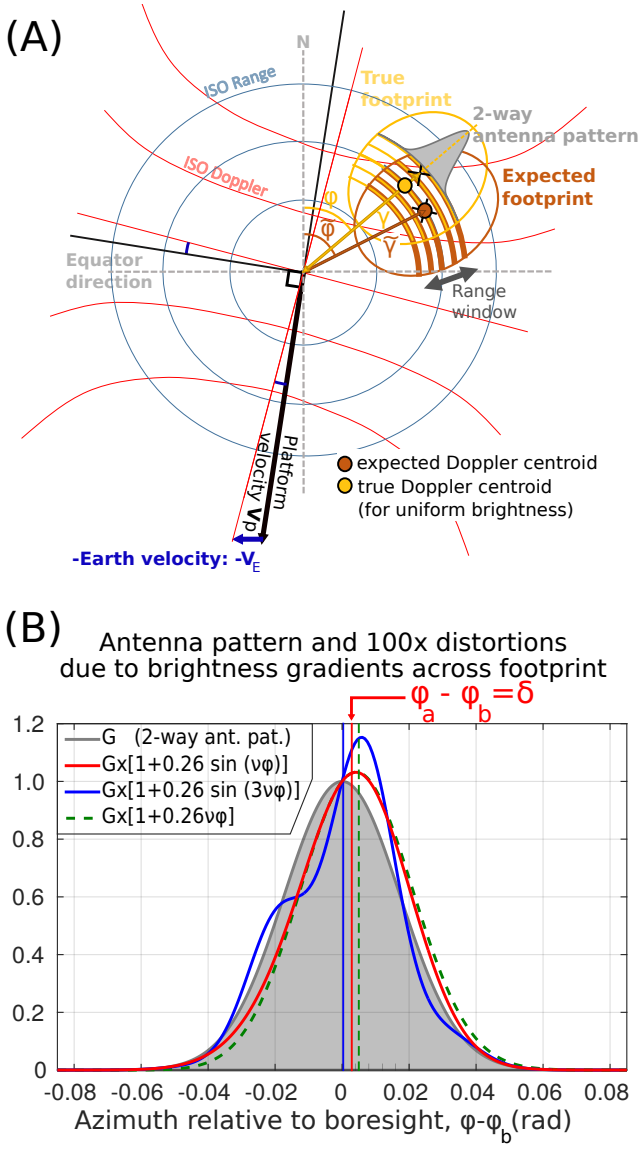

Figure A1. (A) True pointing. The attitude drift changes the antenna footprint direction and shifts the Doppler centroid. Here (γ, φ) are the expected coordinate of the antenna gain ground projection while $(\tilde{\gamma}, \tilde{\varphi})$ are the shifted version of these coordinates by the attitude misknowledge, adapted from Delouis et al.. (B) Apparent pointing φ_a for the SKIM geometry. Examples of 2-way antenna gain G as a function of azimuth and distortions (exaggerated 100 times) induced by σ^0 gradients on the power integrated by the radar in the azimuth direction across the antenna pattern (grey curve). Three examples of asymetric distortions are given: a sine function with $\nu = \sin\theta/\sigma_\alpha$, a 3-times faster varying sine function, and a linear trend. If the azimuth φ correlates with the geometrical Doppler, then the distortion produces an apparent velocity error V_δ which corresponds to an apparent mispointing indicated by the vertical lines.

https://doi.org/10.5194/os-2019-77
Preprint. Discussion started: 27 August 2019


Ocean Science
Discussions
Open Access
EGU

this case $\theta = \arccos(H/r)$. If now the radar suffers from a timing error δr, the instrument will detect a false altitude $H - \delta r$, but will ascribe to range bin $r - \delta r$ the signal coming from r. In the meantime, we consider that the surface-tracking algorithm suffers from an error δh, and detects the surface at range $H - \delta r - \delta h$. The data from this range bin will thus be processed using an angle of incidence

$$\theta + \delta_\theta = \arccos\left(\frac{H - \delta r - \delta h}{r - \delta r}\right), \tag{A23}$$

different from the correct value by

$$\delta_\theta \simeq \frac{1}{\tan(\theta)}\left[\frac{\delta h}{H}\cos(\theta) + \frac{\delta r}{H}\left[1 - \cos(\theta)\right]\right]. \tag{A24}$$

Considering δh and δr as independent, we see that at 12° incidence the incidence knowledge requirements expressed above for SKIM and KuROS translate respectively to timing accuracy requirements of 2.4 m and 0.5 m, and to surface-tracking accuracy requirements of 5.4 cm and 1.14 cm.

The timing accuracy requirements are easily met in the spaceborne context, but can be challenging in the cost-constrained context of an airborne instrument.

The surface-tracking algorithm, however, does not benefit from the error-compensation that exists for the timing error. The requirement for SKIM is stringent, but the SKIM mission comprises a state-of-the-art Ka-band nadir-looking altimeter capable of reaching this goal. The 1.14 cm altitude tracking requirement is clearly out of reach of the KuROS airborne instrument. Our analysis of its Doppler data will thus be restricted to the side-looking configurations for which, as per eq. (A22), the pointing requirements are much milder.

A3.4 Effective pointing / Azimuth Gradient Doppler

As expressed in eq. (A22), for each range resolution cell V_{NG} results from an integral over azimuth with a weight that depends on the product of the antenna radiation diagram and the sea surface NRCS, which varies as a function of the horizontal position (x, y) due to the presence of waves, varying winds, currents, surfactants, sea ice and all the physical properties of the sea surface.

Even with a perfect knowledge of the platform attitude and velocity, NRCS variations can thus make the effective pointing of the measurements deviate from the pure geometric estimates. Valuable insight into this effect can be gained by considering the saddle-point approximation of eq. (A22) in the limit of a very narrow antenna diagram (which is clearly applicable for SKIM and KaRADOC, less so for KuROS).

Considering first the case of an antenna pointing towards azimuth φ_A with an infinitely narrow radiation diagram, we see that the product $W(t_1, r', \varphi)\widetilde{\sigma^0}(t_1, r', \varphi)$ is well approximated by the Dirac distribution $\delta(\varphi - \varphi_A)$. In this limit

$$V_{NG}(t_1, r') = V_R\left[\cos(g)\sin(\theta)\cos(\varphi_A - c) + \sin(g)\cos(\theta)\right]. \tag{A25}$$

We recognize in this expression V_{geo}, the estimate of V_{NG} one would have derived using direct geometric arguments.

https://doi.org/10.5194/os-2019-77
Preprint. Discussion started: 27 August 2019

The essence of the argument is that the sharpest factor in the integral is the beam radiation diagram. If it is now not infinitely sharp, we see that the effet of a gradient of $\widetilde{\sigma^0}$ is to shift the peak of the distribution by an angle

$$\delta = -\frac{\partial_\varphi \log(\widetilde{\sigma^0})\Big|_{\varphi_A}}{\partial_{\varphi\varphi} \log(W)|_{\varphi_A}}. \tag{A26}$$

Assuming for $W(t_1, t', \varphi)$ a Gaussian approximation

$$W(t_1, r', \varphi) = \frac{1}{\sqrt{\pi}\sigma_\varphi(r')} \exp\left[-\frac{(\varphi - \varphi_A)^2}{\sigma_\varphi^2(r')}\right] \tag{A27}$$

in which $\sigma_\varphi(r')$ is a parameter describing the width of the antenna diagram at the working incidence angle, one obtains

$$V_{\mathrm{NG}}(t_1, r') = V_R\left[\cos(g)\sin(\theta)\cos(\varphi_A - c + \delta\varphi)\right. \tag{A28}$$

$$\left. + \sin(g)\cos(\theta)\right]. \tag{A29}$$

with

$$\delta = \frac{\sigma_\varphi^2(r')}{2}\, \partial_\varphi \log(\widetilde{\sigma^0}). \tag{A30}$$

Alternatively, one can choose to express V_{NG} as the sum of V_{geo}, the geometric approximation, plus an Azimuth Gradient Doppler contribution

$$V_{NG}(t_1, r') = V_{geo}(t_1, r') + V_{AGD}(t_1, r'), \tag{A31}$$

with

$$V_{\mathrm{geo}}(t_1, r') = V_R\left[\cos(g)\sin(\theta)\cos(\varphi_A - c) + \sin(g)\cos(\theta)\right] \tag{A32}$$

and

$$V_{\mathrm{AGD}}(t_1, r') = -V_R \cos(g)\sin(\theta)\sin(\varphi_A - c) \tag{A33}$$

$$\times \frac{\sigma_\varphi^2(r')}{2} \partial_\varphi \log(\widetilde{\sigma^0}). \tag{A34}$$

One can see from these expressions that for a given azimuthal variation of the NRCS the order of magnitude of V_{AGD} is set by the width of the antenna radiation diagram: instruments with a thin diagram, such as SKIM and KaRADOC, are less affected than instruments with a broader pattern, such as KuROS. Also, one sees that V_{AGD} is largest when the instrument looks in the cross-track direction, and is zero in the up/down track viewing directions. Finally, one sees that V_{AGD} is equivalent to the line-of-sight projection of a spurious horizontal velocity U_{AGD}, which varies with incidence only through the variations of $\widetilde{\sigma^0}$ and σ_φ:

$$U_{AGD}(t_1, r') = -V_R \sin(\varphi_A - c) \frac{\sigma_\varphi^2(r')}{2} \partial_\varphi \log(\widetilde{\sigma^0}). \tag{A35}$$

https://doi.org/10.5194/os-2019-77
Preprint. Discussion started: 27 August 2019

Ocean Science
Discussions
Open Access
EGU

Appendix B: KuROS antenna pattern determination

A precise determination of the antenna pattern is necessary for any Doppler application, given the possibly large contribution of pointing errors $\varphi_b - \widetilde{\varphi}$ in the estimation of the non-geophysical Doppler, and the effect of the antenna beamwidth in the spurious Azimuth Gradient velocity U_{AGD}. A comprehensive strategy has thus been developed for estimating the 1-way antenna pattern in amplitude and phase, combining anechoic chamber measurements and verification using the campaign data, and final adjustment of systematic phase shifts in the data. (In this section α and β are respectively the latitude and longitude of a set of spherical coordinates centered on the antenna, and such that the main lobe extends in a longitudinal sector on the equator $\alpha = 0$, and the rotation axis of the antenna turntable points towards $\alpha = 0$, $\beta = 0$. With this choice of coordinates the antenna diagram has separable Gaussian dependencies on α and β. In level flight, when the antenna points towards ϕ_A, $\sin(\alpha) = \sin(\theta)\sin(\varphi - \varphi_A)$, $\tan(\beta) = \tan(\theta)\cos(\varphi - \varphi_A)$).

B1 Fixed antenna NRCS correction

The anechoic chamber measurements are very accurate for the antenna alone. However, once integrated into the plane, the antenna pattern is perturbed. This is for instance particularly noticeable in the NRCS measurements in rotating mode, where a spurious azimuthal pattern could clearly be seen, or for fixed-antenna Doppler observations, where a striping pattern is obvious. We have thus developed a complementary method that relies on the variations of the plane attitude during maneuvers. Using the

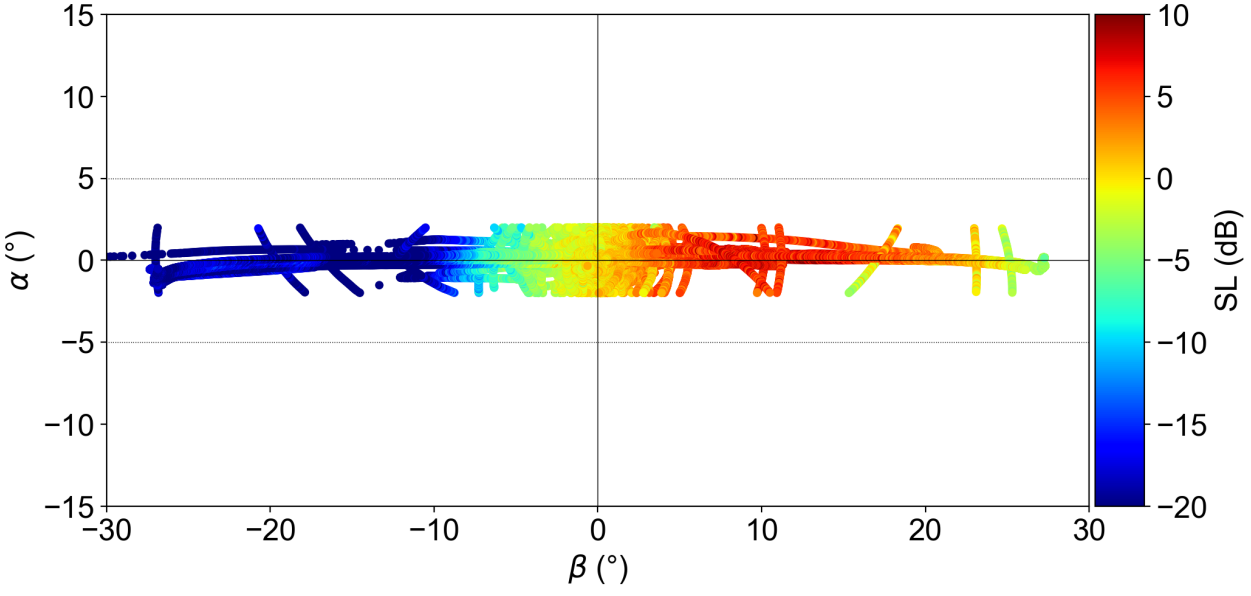

Figure B1. Reconstructed α, β dependence of the 2-way KuROS antenna diagram. For each 30 s data segment, the level flight values, for which the nadir is at $\alpha = 0$, $\beta = 0$, have been used as reference level to account for geophysical variations in nadir NRCS.

https://doi.org/10.5194/os-2019-77
Preprint. Discussion started: 27 August 2019

plane IMU, we identify the angular coordinates α and β of the nadir, and use the measured power to map the antenna pattern (using as a reference point the level flight return power values for each data segment, to account for geophysical nadir NRCS variations). The combination of all the flights during the campaign gives the distribution of measured power as a function of α and β that is shown in Figs. B1 and B2.

The measured distribution is well approximated by a Gaussian shape

$$G(\alpha,\beta) = \exp\left[-\frac{\alpha^2}{2\sigma_\alpha^2} - \frac{(\beta-\beta_0)^2}{2\sigma_\beta^2}\right]. \tag{B1}$$

Another expression for $G(\alpha,\beta)$, more suitable for use with the half-power beamwidths $\alpha_{-3\mathrm{dB}}$ and $\beta_{-3\mathrm{dB}}$ obtained from anechoic chamber measurements, is:

$$G(\alpha,\beta) = 2^{\left[-\frac{4\alpha^2}{\alpha_{-3\mathrm{dB}}^2} - \frac{4(\beta-\beta_0)^2}{\beta_{-3\mathrm{dB}}^2}\right]}. \tag{B2}$$

The width parameters in these equations are linked by

$$\sigma_\alpha = \alpha_{-3\mathrm{dB}}/\sqrt{8\log(2)},\ \sigma_\beta = \beta_{-3\mathrm{dB}}/\sqrt{8\log(2)}$$

The parameter values used in this study are collected in table 1.

One cautionary remark is that the illuminated patch at nadir is not infinitely sharp. The measured distribution is thus the convolution of the true antenna diagram by the power distribution at the nadir patch (which depends on the altitude tracking error as well as the sea state (Chelton et al., 1989)). Assuming Gaussian shapes, the squares of the width parameters add, leading to

$$\sigma_{observed} \simeq \sigma_{true}\left[1 + \frac{\sigma_{patch}^2}{2\sigma_{true}^2}\right].$$

The broadening of the diagram due to finite nadir patch size is thus a small correction provided the scale of the nadir patch remains smaller than the antenna diagram scales. For reasonable orders of magnitude of the altitude tracking error and significant wave height, the patch -3 dB width is of the order of 3° when viewed from 3000 m height. This corresponds to a 3% correction on the value of σ_α. We have chosen to neglect this correction. The values summarized in table 1 are the parameters of the Gaussian fits to the observed distributions.

B2 Rotating antenna NRCS correction

Using these parameters as a starting point, we have then constructed corrections for the rotating antenna measurements of NRCS, by allowing the boresight elevation β_0 to vary as a function of antenna orientation within the plane. The variation law was determined by minimizing the dependence of the rotating-antenna NRCS measurements as a function of flight direction over the Offshore box for each day.

https://doi.org/10.5194/os-2019-77
Preprint. Discussion started: 27 August 2019

Ocean Science
Discussions
Open Access
EGU

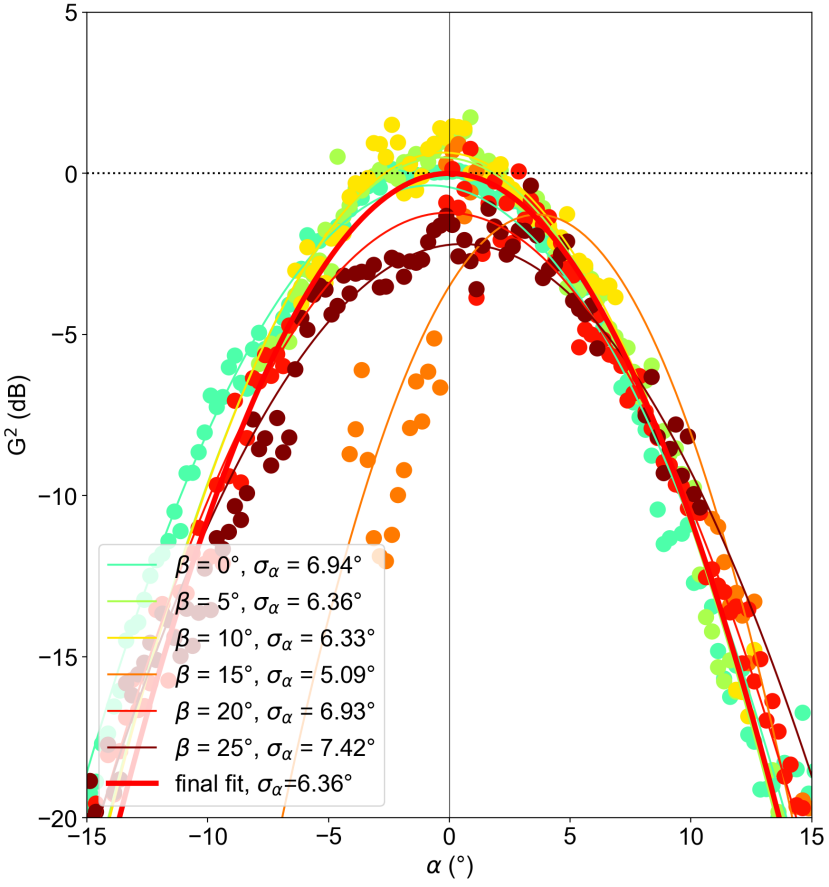

Figure B2. Reconstructed azimuth dependence of nadir return power for different incidence angles. For each incidence angle, the $\alpha = 0$ value has been used as a reference. The thick line shows the final Gaussian fit used in the data analysis. The $\beta = 15^{\circ}$ data were excluded from the fit.

B3 Fixed antenna Doppler correction

In a similar way, we have observed that the KuROS antenna diagram is slightly "wrinkled", in that the beam boresight azimuth changes as a function of elevation. This azimuthal mispointing transposes immediately into a striping modulation of the U_{GD} estimates. A correction was introduced by allowing the boresight azimuth α_0 to vary as a function of β. The variation law of α_0 was determined by minimizing the average U_{GD} over all flights for each value of β. As the variation of this quantity with respect to $\alpha_0(\beta)$ is not trivial, this required constructing, regularizing and inverting the observation matrix.

https://doi.org/10.5194/os-2019-77
Preprint. Discussion started: 27 August 2019

Ocean Science
Discussions
Open Access
EGU

Appendix C: KaRADOC system

KaRADOC is built around an Agilent PNA-X network analyzer, complemented by a TX power amplifier, a T/R switch, a RX low-noise amplifier, and a high-gain purpose-built slotted waveguide antenna (shown in Fig. C1).

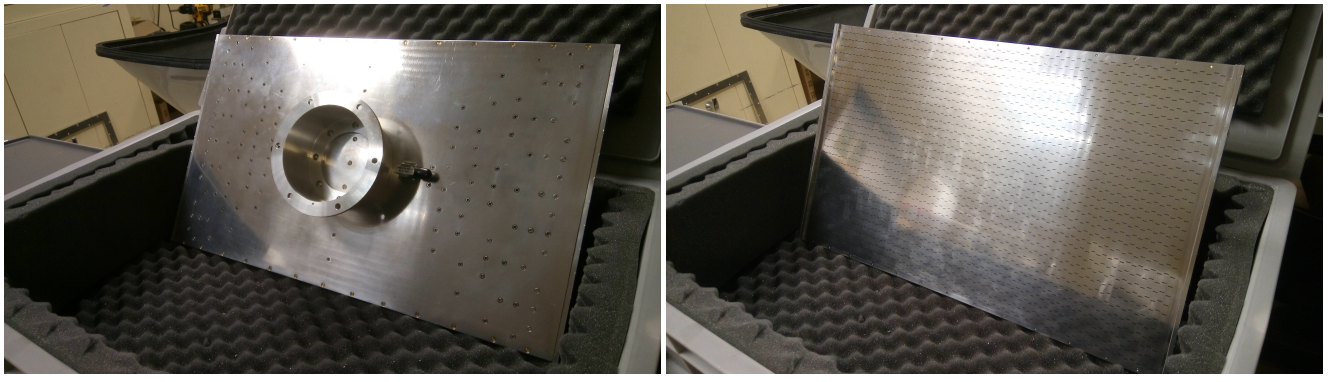

Figure C1. The back (on the left) and the front (on the right) of the antenna

The beam can be steered in elevation by changing the instrument working frequency (see Fig. C2A). For the Drift4SKIM experiment, the antenna was mounted in a port-looking configuration, centered on 10° incidence, with a 2° backward-looking tilt to compensate for the aircraft pitch in level flight. Observations at 12° were collected at 33.7 GHz. Other angles were also scanned, but RF leakage from the TX to the RX subsystems was too strong at the corresponding frequencies, making the signal harder to analyze.

The antenna radiation diagram is very narrow, with a beamwidth less than 1.5° in elevation and less than 2° in azimuth (see Fig. C2B). Figures C3A and C3B) represent sections across the KaRADOC main lobe in the azimuth and elevation direction, at 33.7 GHz.

https://doi.org/10.5194/os-2019-77
Preprint. Discussion started: 27 August 2019

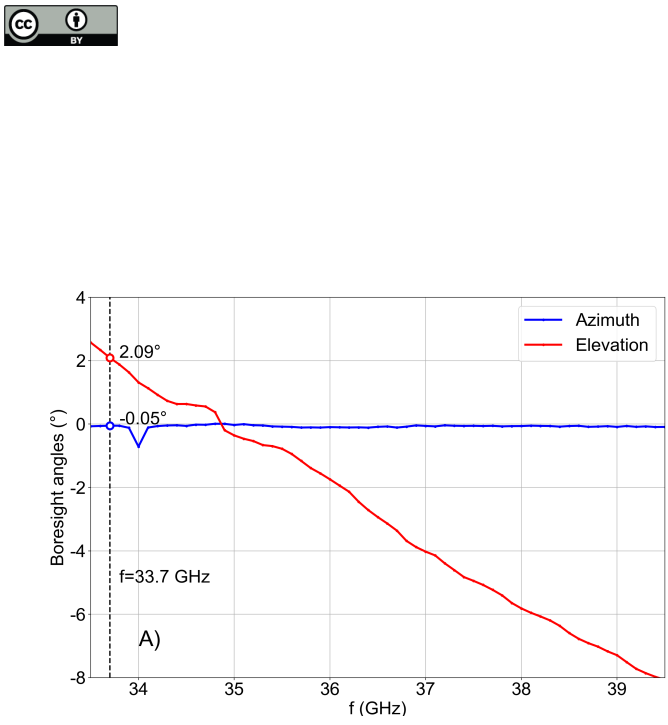

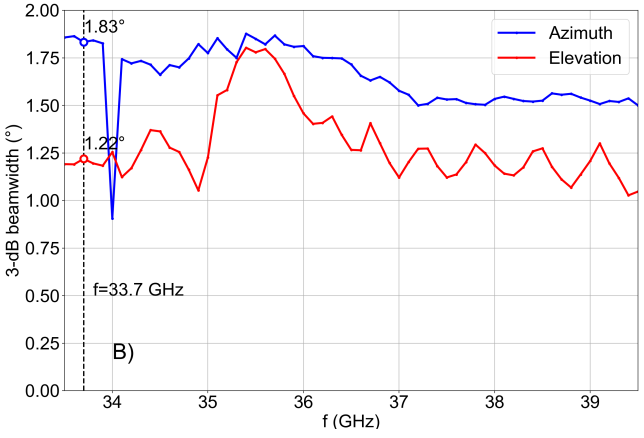

Figure C2. Frequency dependence of the KaRADOC main lobe azimuth and elevation boresight angles (A) and half-power beamwidths (B).

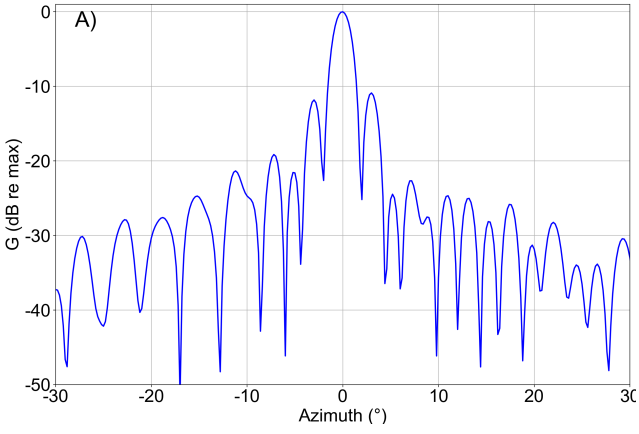

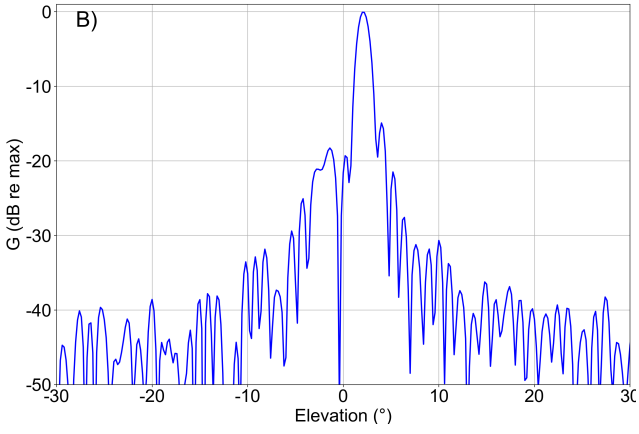

Figure C3. KaRADOC radiation diagram at 33.7 GHz as a function of (A) azimuth at 2.09° elevation and (B) elevation at -0.05° azimuth.

https://doi.org/10.5194/os-2019-77
Preprint. Discussion started: 27 August 2019

Author contributions. All authors have contributed to the writing of the paper..

Competing interests. The authors declare that they have no conflict of interest.

Disclaimer. The views and opinions expressed in this publication can in no way be taken to reflect the official opinion of the European Space Agency.

Acknowledgements. This study was supported by the KuROS4SKIM and DRIFT4SKIM contracts from the European Space Agency, made possible by the unflagging determination of Erik de Witte. The in situ measurements owe much to the dedication of the R/V Thalia crew. Airborne data was obtained using the aircraft managed by Safire, the French facility for airborne research, an infrastructure of the French National Center for Scientific Research (CNRS), Météo-France and the French National Center for Space Studies (CNES). Many people at LOPS and OceanDataLab also contributed to the preparation, deployment and recovery of the instruments, including Peter Sutherland, Mickael Accensi, Sylvain Herledan, Gilles Guitton, Lucile Gaultier, Michel Hamon, Olivier Péden, Stéphane Leizour, Pierre Branellec. Many people at IETR are involved in the KaRADOC developments: Cécile Leconte, Mohamed Himdi, Paul leroy, Eric Pottier and especially Guy Grunfelder and Mor Diama Lo who have made possible the measurement campaign during November, 2018. Operation of KuROS during the experiment would not have been possible without the dedication of Christophe Le Gac, Nicolas Pauwels and Christophe Dufour, from CNRS/LATMOS.

https://doi.org/10.5194/os-2019-77
Preprint. Discussion started: 27 August 2019

References

Ardhuin, F., Marié, L., Rascle, N., Forget, P., and Roland, A.: Observation and estimation of Lagrangian, Stokes and Eulerian currents induced by wind and waves at the sea surface, J. Phys. Oceanogr., 39, 2820–2838, doi:10.1175/2009JPO4169.1, http://journals.ametsoc.org/doi/pdf/10.1175/2009JPO4169.1, 2009.

Ardhuin, F., Balanche, A., Stutzmann, E., and Obrebski, M.: From seismic noise to ocean wave parameters: general methods and validation, J. Geophys. Res., 117, C05 002, doi:10.1029/2011JC007449, 2012.

Ardhuin, F., Aksenov, Y., Benetazzo, A., Bertino, L., Brandt, P., Caubet, E., Chapron, B., Collard, F., Cravatte, S., Dias, F., Dibarboure, G., Gaultier, L., Johannessen, J., Korosov, A., Manucharyan, G., Menemenlis, D., Menendez, M., Monnier, G., Mouche, A., Nouguier, F., Nurser, G., Rampal, P., Reniers, A., Rodriguez, E., Stopa, J., Tison, C., Tissier, M., Ubelmann, C., van Sebille, E., Vialard, J., and Xie, J.: Measuring currents, ice drift, and waves from space: the Sea Surface KInematics Multiscale monitoring (SKIM) concept, Ocean Sci., 14, 337–354, doi:10.5194/os-2017-65, 2018.

Ardhuin, F., Chapron, B., Maes, C., Romeiser, R., Gommenginger, C., Cravatte, S., Morrow, R., Donlon, C., and Bourassa, M.: Satellite Doppler observations for the motions of the oceans, Bull. Amer. Meterol. Soc., 100, doi:10.1175/BAMS-D-19-0039.1, 2019.

Barrick, D. E. and Weber, B. L.: On the nonlinear theory for gravity waves on the ocean's surface. Part II: Interpretation and applications, J. Phys. Oceanogr., 7, 3–10, http://ams.allenpress.com/archive/1520-0485/7/1/pdf/i1520-0485-7-1-11.pdf, 1977.

Barrick, D. E., Headrick, J. M., Bogle, R. W., and Crombie, D. D.: Sea backscatter at HF: interpretation and utilization of the echo, Proc. IEEE, 62, 673, 1974.

Broche, P., de Maistre, J. C., and Forget, P.: Mesure par radar décamétrique cohérent des courants superficiels engendrés par le vent, Oceanol. Acta, 6, 43–53, 1983.

Buck, C.: An extension to the wide swath ocean altimeter concept, in: Proceedings of the IEEE International Geoscience and Remote Sensing Symposium (IGARSS), 2005., vol. 8, pp. 543–5439, IEEE, doi:10.1109/IGARSS.2005.1525970, 2005.

Buck, C., Aguirre, M., Donlon, C., Petrolati, D., and D'Addio, S.: Steps towards the preparation of Wavemill mission, in: Proceedings of the IEEE International Geoscience and Remote Sensing Symposium (IGARSS), 2011, pp. 3959–3962, IEEE, doi:10.1109/igarss.2011.6050098, 2011.

Caudal, G., Hauser, D., Valentin, R., and Gac, C. L.: KuROS: A New Airborne Ku-Band Doppler Radar for Observation of Surfaces, J. Atmos. Ocean Technol., 31, 2023–2245, doi:10.1175/JTECH-D-14-00013.1, 2014.

Chapron, B., Vandemark, D., and Elfouhaily, T.: On the skewness of the sea slope probability distribution, in: Gas transfer at water surfaces, edited by Donelan, M. A., Drennan, W. M., Saltzman, E. S., and Wanninkhof, R., vol. 127 of *Geophys. Monogr. Ser.*, pp. 59–63, American Geophysical Union, doi:10.1029/GM127p0059, 2002.

Chapron, B., Collard, F., and Ardhuin, F.: Direct measurements of ocean surface velocity from space: interpretation and validation, J. Geophys. Res., 110, doi:10.1029/2004JC002809, 2005.

Chelton, D. B., Walsh, E. J., and MacArthur, J. L.: Pulse compression and sea level tracking in satellite altimetry, J. Atmos. Ocean Technol., 6, 407–438, doi:10.1175/1520-0426(1989)006<0407:pcaslt>2.0.co;2, 1989.

Chelton, D. B., Schlax, M. G., Samelson, R. M., Farrar, J. T., Molemaker, M. J., and Gula, J. C. M. J.: Prospects for Future Satellite Estimation of Small-Scale Variability of Ocean Surface Velocity and Vorticity, Progress in Oceanography, 173, 256–350, doi:10.1016/j.pocean.2018.10.012, 2019.

https://doi.org/10.5194/os-2019-77
Preprint. Discussion started: 27 August 2019

Elfouhaily, T. M.: A consistent wind and wave model and its application to microwave remote sensing of the ocean surface, Ph.D. thesis, Denis Diderot University, Paris, 1997.

ESA: Report for Mission Selection: SKIM, Tech. Rep. ESA-EOPSM-SKIM-RP-3550, European Space Agency, Noordwijk, The Netherlands, doi:10.13140/RG.2.2.22907.98081/3, 2019.

Guimaraes, P. V., Ardhuin, F., Sutherland, P., Accensi, M., Hamon, M., Pérignon, Y., Thomson, J., Benetazzo, A., and Ferrant, P.: A Surface KInematics Buoy (SKIB) for wave-current interactions studies, Ocean Sci., doi:10.5194/os-2018-45, 2018.

Gurgel, K. W. and Barbin, Y. .: Suppressing radio frequency Interference in HF radars, Sea Technology, 49, 39–42, 2008.

Gurgel, K.-W., Antonischki, G., Essen, H.-H., and Schlick, T.: Wellen Radar (WERA), a new ground-wave based HF radar for ocean remote sensing, Coastal Eng., 37, 219–234, doi:10.1016/S0378-3839(99)00027-7, 1999.

Hansen, M. W., Johannessen, J. A., Dagestad, K. F., Collard, F., and Chapron, B.: Monitoring the surface inflow of Atlantic Water to the Norwegian Sea using Envisat ASAR, J. Geophys. Res., 116, C12 008, doi:10.1029/2011JC007375, 2011.

Hauser, D., Tison, C., Amiot, T., Delaye, L., Corcoral, N., and Castillan, P.: SWIM: The First Spaceborne Wave Scatterometer, IEEE Trans. on Geosci. and Remote Sensing, 55, 3000–3014, 2017.

Jackson, F. C., Walton, W. T., and Baker, P. L.: Aircraft and satellite measurement of ocean wave directional spectra using scanning-beam microwave radars, J. Geophys. Res., 90, 987–1004, 1985.

Kenyon, K. E.: Stokes drift for random gravity waves, J. Geophys. Res., 74, 6991–6994, 1969.

Kudryavtsev, V., Yurovskaya, M., Chapron, B., Collard, F., and Donlon, C.: Sun glitter Imagery of Surface Waves. Part 1: Directional spectrum retrieval and validation, J. Geophys. Res., 122, doi:10.1002/2016JC012425, 2017.

Kuik, A. J., van Vledder, G. P., and Holthuijsen, L. H.: A method for the routine analysis of pitch-and-roll buoy wave data, J. Phys. Oceanogr., 18, 1020–1034, http://journals.ametsoc.org/doi/pdf/10.1175/1520-0485%281987%29017%3C0845%3ATROWDT%3E2.0.CO%3B2, 1988.

Lazure, P. and Dumas, F.: An external-internal mode cou- pling for a 3D hydrodynamical model for applications at regional scale (MARS)., Adv. Water Resour., 31, 233–250, 2008.

Le Boyer, A., Cambon, G., Daniault, N., Herbette, S., Cann, B. L., Marié, L., and Morin, P.: Observations of the Ushant tidal front in September 2007, Continental Shelf Research, 18, in press, 2009.

LOPS: Estimation of Non-Geophysical Doppler and Wave Doppler, and inversion algorithm for SKIM, Tech. Rep. SKIM-MPRC-TN5-V1.5-LOPS-2019, ESA, doi:10.13140/RG.2.2.22907.98081/3, 2019.

Lygre, A. and Krogstad, H. E.: Maximum entropy estimation of the directional distribution in ocean wave spectra, J. Phys. Oceanogr., 16, 2,052–2,060, 1986.

Martin, A. C. H., Gommenginger, C., Marquez, J., Doody, S., Navarro, V., and Buck, C.: Wind-wave-induced velocity in ATI SAR ocean surface currents: First experimental evidence from an airborne campaign, J. Geophys. Res., 121, 1640–1653, doi:10.1002/2015JC011459, 2016.

Martin, A. C. H., Gommenginger, C. P., and Quilfen, Y.: Simultaneous ocean surface current and wind vectors retrieval with squinted SAR interferometry: Geophysical inversion and performance assessment, Remote sensing of Environment, 216, 798–808, doi:10.1016/j.rse.2018.06.013, 2018.

Munk, W.: An Inconvenient Sea Truth: Spread, Steepness, and Skewness of Surface Slopes, Annu. Rev. Mar. Sci., 1, 377–415, doi:n10.1146/annurev.marine.010908.163940, 2008.

https://doi.org/10.5194/os-2019-77
Preprint. Discussion started: 27 August 2019

Niiler, P. P. and Paduan, J. D.: Wind-driven motions in the Northeast Pacific as measured by Lagrangian drifters, J. Phys. Oceanogr., 25, 2819–2930, http://ams.allenpress.com/archive/1520-0485/25/11/pdf/i1520-0485-25-11-2819, 1995.

Nouguier, F.: Remote Sensing Spatial Simulator (R3S), Tech. Rep. SKIM-MPRC-TN6-V1.0-LOPS-2019, ESA, 2019.

Nouguier, F., Guérin, C.-A., and Chapron, B.: "Choppy wave" model for nonlinear gravity waves, J. Geophys. Res., 114, C09 012, doi:10.1029/2008JC004984, 2009.

Nouguier, F., Chapron, B., and Guérin, C.-A.: Second-order Lagrangian description of tri-dimensional gravity wave interactions, J. Geophys. Res., 114, C09 012, doi:10.1029/2008JC004984, 2015.

Nouguier, F., Mouche, A., Rascle, N., Chapron, B., and Vandemark, D.: Analysis of Dual-Frequency Ocean Backscatter Measurements at Ku- and Ka-Bands Using Near-Nadir Incidence GPM Radar Data, IEEE Geoscience And Remote Sensing Letters, 31, 2023–2245, doi:10.1109/LGRS.2016.2583198, 2016.

Nouguier, F., Chapron, B., Collard, F., Mouche, A., Rascle, N., Ardhuin, F., and Wu, X.: Sea surface kinematics from near-nadir radar measurements, IEEE Trans. on Geosci. and Remote Sensing, 56, 6169–6179, doi:10.1109/TGRS.2018.2833200, http://tiny.cc/SKIMonRG_NOUG, 2018.

Novelli, G., Guigand, C. M., Cousin, C., Ryan, E. H., Laxague, N. J. M., Dai, H., Haus, B. K., and Özgökmen, T. M.: A Biodegradable Surface Drifter for Ocean Sampling on a Massive Scale, J. Atmos. Ocean Technol., 34, 2509–2532, doi:10.1175/JTECH-D-17-0055.1, 2017.

Peureux, C., Benetazzo, A., and Ardhuin, F.: Note on the directional properties of meter-scale gravity waves, Ocean Science, 14, 41–52, doi:10.5194/os-14-41-2018, 2018.

Rodriguez, E.: On the Optimal Design of Doppler Scatterometers, Remote Sensing, 10, 1765, doi:doi:10.3390/rs10111765, 2018.

Rodríguez, E., Wineteer, A., Perkovic-Martin, D., Gál, T., Stiles, B. W., Niamsuwan, N., and Monje, R. R.: Estimating Ocean Vector Winds and Currents Using a Ka-Band Pencil-Beam Doppler Scatterometer, Remote Sensing, 4, 576, doi:10.3390/rs10040576, 2018.

Roland, A. and Ardhuin, F.: On the developments of spectral wave models: numerics and parameterizations for the coastal ocean, Ocean Dynamics, 64, 833–846, doi:10.1007/s10236-014-0711-z, 2014.

Romeiser, R., Breit, H., Eineder, M., Runge, H., Flament, P., de Jong, K., and Vogelzang, J.: On the Suitability of TerraSAR-X Split Antenna Mode for Current Measurements by Along-Track Interferometry, in: Proceedings of the IGARSS conference, Toulouse, France, 2003.

Rouault, M. J., Mouche, A., Collard, F., Johannessen, J. A., and Chapron, B.: Mapping the Agulhas Current from space: An assessment of ASAR surface current velocities, J. Geophys. Res., 115, C10 026, doi:10.1029/2009JC006050, 2010.

Sandwell, D. T. and Smith, W. H. F.: Slope correction for ocean radar altimetry., Journal of Geodesy, 88, 765–771, doi:10.1007/s00190-014-0720-1, 2014.

Stewart, R. H. and Joy, J. W.: HF radio measurements of surface currents, Deep Sea Res., 21, 1039–1049, 1974.

Stopa, J. E., Ardhuin, F., Bababin, A., and Zieger, S.: Comparison and validation of physical wave parameterizations in spectral wave models, Ocean Modelling, 103, 2–17, doi:10.1016/j.ocemod.2015.09.003, 2016.

Sudre, J., Maes, C., and Garçon, V.: On the global estimates of geostrophic and Ekman surface currents, Limnology and Oceanography: Fluids and Environments, 3, 1–20, doi:10.1215/21573689-2071927, 2013.

Sutherland, G., Marié, L., Reverdin, G., Christensen, K. H., Broström, G., and Ward, B.: Enhanced Turbulence Associated with the Diurnal Jet in the Ocean Surface Boundary Layer, J. Phys. Oceanogr., 46, 3051–3067, doi:10.1175/JPO-D-15-0172.1, 2016.

Sutherland, P. and Brozena, J.: Airborne remote sensing of wave propagation in the marginal ice zone, J. Geophys. Res., 123, in press, 2018.

https://doi.org/10.5194/os-2019-77
Preprint. Discussion started: 27 August 2019

Walsh, E. J., Hancock, III, D. W., Hines, D. E., Swift, R. N., and Scott, J. F.: An observation of the directional wave spectrum evolution from shoreline to fully developed, J. Phys. Oceanogr., 17, 1288–1295, http://ams.allenpress.com/archive/1520-0485/19/5/pdf/i1520-0485-19-5-1288.pdf, 1989.

Walsh, E. J., Banner, M. L., Wright, C. W., Vandemark, D. C., Chapron, B., Jensen, J., and Lee, S.: The Southern Ocean Waves Experiment. Part III: Sea Surface Slope Statistics and Near-Nadir Remote Sensing, J. Phys. Oceanogr., 38, 670–685, doi:10.1175/2007JPO3771.1, 2008.

Yueh, S. H., Tang, W., Fore, A. G., Neumann, G., Hayashi, A., Freedman, A., Chaubell, J., and Lagerloef, G. S. E.: L-Band Passive and Active Microwave Geophysical Model Functions of Ocean Surface Winds and Applications to Aquarius Retrieval, IEEE Trans. on Geosci. and Remote Sensing, 51, 4619–4632, 2013.

Yurovsky, Y. Y., Kudryavtsev, V. N., Grodsky, S. A., and Chapron, B.: Sea Surface Ka-Band Doppler Measurements: Analysis and Model Development, Remote Sensing, 11, 839, doi:10.3390/rs11070839, 2019.

Zrnic, D. S.: Spectral Moment Estimates from Correlated Pulse Pairs, IEEE Trans. Aero. Electronic Sys., 13, 344–354, doi:10.1109/TAES.1977.308467, 1977.